Spectral Evidence for Heating at Large Column Mass in Umbral Solar Flare Kernels. I. *IRIS* Near-UV Spectra of the X1 Solar Flare of 2014 October 25

Adam F. Kowalski[1,2,3] , Elizabeth Butler[1], Adrian N. Daw[4] , Lyndsay Fletcher[5,6], Joel C. Allred[4] , Bart De Pontieu[6,7,8],
Graham S. Kerr[4] , and Gianna Cauzzi[2]

[1] Department of Astrophysical and Planetary Sciences, University of Colorado Boulder, 2000 Colorado Avenue, Boulder, CO 80305, USA
adam.f.kowalski@colorado.edu
[2] National Solar Observatory, University of Colorado Boulder, 3665 Discovery Drive, Boulder, CO 80303, USA
[3] Laboratory for Atmospheric and Space Physics, University of Colorado Boulder, 3665 Discovery Drive, Boulder, CO 80303, USA
[4] NASA Goddard Space Flight Center, Heliophysics Sciences Division, Code 671, 8800 Greenbelt Road, Greenbelt, MD 20771, USA
[5] SUPA School of Physics & Astronomy, University of Glasgow, Glasgow, G12 8QQ, UK
[6] Rosseland Centre for Solar Physics, University of Oslo, P.O. Box 1029 Blindern, NO-0315 Oslo, Norway
[7] Lockheed Martin Solar and Astrophysics Laboratory, Org. A021S, Bldg. 252, 3251 Hanover Street, Palo Alto, CA 94304, USA
[8] Institute of Theoretical Astrophysics, University of Oslo, P.O. Box 1029, Blindern, Oslo, Norway
Received 2019 February 24; revised 2019 May 3; accepted 2019 May 5; published 2019 June 21

Abstract

The *GOES* X1 flare SOL2014-10-25T17:08:00 was a three-ribbon solar flare observed with the *Interface Region Imaging Spectrograph* (*IRIS*) in the near-UV (NUV) and far-UV. One of the flare ribbons crossed a sunspot umbra, producing a dramatic, $\sim$1000% increase in the NUV continuum radiation. We comprehensively analyze the UV spectral data of the umbral flare brightenings, which provide new challenges for radiative$-$hydrodynamic modeling of the chromospheric velocity field and the white-light continuum radiation. The emission line profiles in the umbral flare brightenings exhibit redshifts and profile asymmetries, but these are significantly smaller than in another, well-studied X-class solar flare. We present a ratio of the NUV continuum intensity to the Fe II λ2814.45 intensity. This continuum-to-line ratio is a new spectral diagnostic of significant heating at high column mass $(\log m/[\mathrm{g\,cm^{-2}}] > -2)$ during solar flares because the continuum and emission line radiation originate from relatively similar temperatures but moderately different optical depths. The full spectral readout of these *IRIS* data also allow for a comprehensive survey of the flaring NUV landscape: in addition to many lines of Fe II and Cr II, we identify a new solar flare emission line, He I λ2829.91 (as previously identified in laboratory and early-type stellar spectra). The *Fermi*/GBM hard X-ray data provide inputs to radiative$-$hydrodynamic models (which will be presented in Paper II) in order to better understand the large continuum-to-line ratios, the origin of the white-light continuum radiation, and the role of electron beam heating in the low atmosphere.

Key words: stars: flare – Sun: flares

1. Introduction

Flares result from a sudden magnetic reconfiguration in the atmosphere of a star, producing electrons and protons that stream at near the speed of light along the directions of the reconfigured magnetic fields. The flare is a burst of electromagnetic radiation and is thought to be the result of the impact of the (mildly) relativistic electrons ("beams") with the lower, dense stellar atmosphere; the protons and ions produce nonthermal gamma-ray emission (Murphy et al. 1997; Hurford et al. 2006), but their relative contributions to the multi-thermal response has not yet been established. The pan-chromatic continuum radiation, excluding the X-rays, extreme-ultraviolet (EUV), gamma-rays, and radio emission, is collectively known as the white-light continuum radiation because it appears in broadband.[9] The white light is typically one of the most impulsive signatures in a solar flare (e.g., Hudson et al. 2006; Fletcher et al. 2007; Namekata et al. 2017; Watanabe et al. 2017)

and is spatially and temporally correlated with the hard X-rays from the nonthermal electrons on the Sun (Kane et al. 1985; Hudson et al. 1992; Martínez Oliveros et al. 2012).

A common assumption is that the white light originates from increased photospheric (or upper photospheric) radiation. However, chromospheric condensations (Livshits et al. 1981; Fisher 1989; Kowalski et al. 2015b) with low continuum optical depth also produce broadband continuum radiation with a large jump in flux near the hydrogen Balmer limit (Gan et al. 1992; Kowalski et al. 2017a). The capability to test model predictions of the Balmer jump in solar flares has largely disappeared, which is unfortunate because spectra of solar flares in the 1980s (primarily from the Universal Spectrograph) exhibit a variety of characteristics in the Balmer jump spectral region (Acampa et al. 1982; Hiei 1982; Neidig 1983; Donati-Falchi et al. 1984, 1985; Boyer et al. 1985; Kowalski et al. 2015a; Procházka et al. 2017), and we now have methods to model opacity from blended lines and dissolved levels (Uitenbroek 2001; Kowalski et al. 2015b). Therefore, we must employ other spectral diagnostics that critically test these models and constrain whether the white light results from photospheric heating, as suggested by a recent off-limb measurement of the emission height (Martínez Oliveros et al. 2012; but see Battaglia & Kontar 2011; Krucker et al. 2015), primarily from chromospheric heating, or significant heating throughout several layers of the lower atmosphere (Neidig et al. 1993a, 1993b; Kleint et al. 2016). Direct measurements of the

---

[9] Various loose definitions of a "white-light flare" exist, including a flare that could be detected by the eye (which is broadband). In dMe stars, *U*-band flares are certainly considered white-light flares even though our eye is not sensitive to these wavelengths, and flares detected in a narrow passband of the *Solar Dynamics Observatory* (*SDO*)/Helioseismic and Magnetic Imager (HMI) are often called white-light flares, assuming that continuum radiation is the source of the HMI increase. Generally, a white-light flare is a flare that produces a change in continuum radiation that could be detected in the Johnson *U* and/or *V* bands.

white-light emission heights in limb flares may be partially occulted (H. Hudson 2014, private communication), and these events are generally difficult to compare to 1D plane-parallel flare models (but see Heinzel et al. 2017). The specific continuum intensity over a narrow wavelength range has also been used to test electron beam heating in the lower atmosphere (Heinzel & Kleint 2014; Kowalski et al. 2017a). However, the interpretation of the measured intensity can be degenerate since an optically thin continuum source with $T \sim 10^4$ K produces a radiation temperature of 4000–6000 K in the optical (Kowalski & Allred 2018) and nearly 7000 K in the near-UV (NUV) (Kleint et al. 2016). Furthermore, the white-light sources may be unresolved even with current high spatial resolution capabilities (Krucker et al. 2011; Sharykin & Kosovichev 2014; Kowalski et al. 2015a).

Is the photosphere heated to produce an observable amount of continuum radiation that overpowers the chromospheric flare radiation? Evidence for very deep heating exists in dMe flares from the Balmer continuum radiation that is produced in absorption (Kowalski et al. 2013) or in emission[10] with a relatively small jump in continuum flux in the Balmer jump spectral region (Hawley & Pettersen 1991; Hawley & Fisher 1992; Kowalski et al. 2013, 2016, 2019). The mass column density[11] (hereafter, "column mass") that is heated to $T \sim 10,000$ K to reproduce these spectral properties is far smaller than the dMe photospheric column mass of $\log m/[\mathrm{g\,cm}^{-2}] \sim 1$ (Cram & Woods 1982; Kowalski et al. 2017b). In solar and dMe electron beam simulations that produce a flare chromosphere that is optically thin to Balmer and Paschen continuum radiation, radiative backwarming heats the (upper) photosphere but the temperature increase in these deep layers is only $\Delta T \sim 500$–1000 K (Allred et al. 2005, 2006; Cheng et al. 2010), and is not enough to explain the 10,000 K blackbody-like radiation in dMe flares (see also Kowalski et al. 2018). Furthermore, it takes some time ($\Delta t \gtrsim 10$ s; Appendix of Kowalski et al. 2017a) for the solar photosphere to heat up in these models, and it is not clear if beam heating persists in a given flare loop for such long timescales (Aschwanden et al. 1998a; Nishizuka et al. 2009; Penn et al. 2016). Nonthermal electrons exhibit a power law with most electrons at $E \sim 20$ keV; if produced in the corona (as implied by hard X-ray, energy-dependent timing differences; Aschwanden et al. 1995, 1996a, 1996b, 1996c, 1998b; Aschwanden & Schwartz 1995; Aschwanden 1996), most of the electron beam energy is expected to be lost in the mid-to-upper chromosphere ($\log m \sim -3$ to -5; Vernazza et al. 1981). If electron beam heating is shown insufficient to explain impulsive, large temperature increases in the photosphere or low chromosphere, then there must be additional, important sources of heating in flares, such as Alfvén waves (Russell & Fletcher 2013; Kerr et al. 2016; Reep & Russell 2016; Reep et al. 2018) or proton beams (Zharkova & Zharkov 2007; Procházka et al. 2018). Instead of Balmer jump ratio measurements, we must consider other spectral signatures that indicate significant heating at large column mass in solar flares. Additional heating mechanisms at large column mass would be transformative improvements to the standard solar flare model and would have important implications for the heating sources

in superflares in other stars and the young Sun (e.g., Maehara et al. 2012; Osten et al. 2016).

To determine whether low-energy electron beams are sufficient to explain the heating in the low atmosphere, we present a new measurement that can be obtained from spectra with limited wavelength coverage, as is often the case with solar imaging spectrometers. This new measurement is the ratio of the NUV continuum to the Fe II line intensity. The NUV continuum-to-line ratio will be compared directly to radiative–hydrodynamic modeling in Paper II of this series to infer the largest (deepest) column mass that is heated by energetic electrons (or other energy transport mechanisms) in a flare. The flare we study is the X1 flare on 2014 October 25, which produced ribbons that crossed the slit of the *Interface Region Imaging Spectrograph* (*IRIS*) during a hard X-ray event, and occurred during the decay phase of the *GOES* X1 event.

The paper is outlined as follows. In Section 2 we describe the *IRIS* and the *Fermi*/GBM (Gamma-Ray Burst Monitor) data for the X1 flare. In Section 3, we describe the properties of the NUV continuum enhancements, the Fe II $\lambda 2814.45$ line profiles, and the ratios between the NUV continuum intensity and Fe II $\lambda 2814.45$ line-integrated intensity. In Section 4, we describe other characteristics of this flare that are important for radiative–hydrodynamic modeling: a line of He I that has not yet been seen in solar flare spectra and the nonthermal electron power and spectral index inferred from hard X-rays. In Section 5, we summarize our findings and compare the NUV spectral properties to the modeling and *IRIS* observations of another well-studied X-class flare. In Section 6, we conclude with several general implications from these unique solar flare spectra. Appendix A describes the continuum-to-line ratio dependence on the temperature and density in optically thin slab model approximations, and Appendix B contains identifications of observed flare lines in the *IRIS* NUV and discussion of the observational constraints they provide for models.

2. Data

The 2014 October 25 X1 solar flare was observed with a unique data set that included a custom *IRIS* observing mode, which is described in Section 2.1. Hard X-ray observations were provided by *Fermi*/GBM throughout the entire flare as well (Section 2.2). This comprehensive data set allows us to test radiative-hydrodynamic (RHD) modeling of electron beam heating in new ways (in Paper II).

2.1. IRIS *Ultraviolet Data*

IRIS (De Pontieu et al. 2014) observed the *GOES* X1 flare SOL2014-10-25T17:08:00 ($\mu = 0.85$, $x = 408''$, $y = -318''$) from National Oceanic and Atmospheric (NOAA) Active Region (AR) 12192. The X-class flares from AR 12192 have been studied extensively due to the absence of associated coronal mass ejections (Thalmann et al. 2015; Inoue et al. 2016; Bamba et al. 2017; Amari et al. 2018). The *IRIS* spectra of the 2014 October 25 X1 flare were obtained in a "sit-and-stare" mode with an exposure time of 4 s, a temporal cadence of 5.4 s, and the slit oriented in the E–W direction. The slit jaw images (SJIs) in the Mg II *h* wing (hereafter SJI 2832), C II, and Mg II were obtained with a cadence of 16 s. All spectra and SJIs were calibrated from DN s^{-1} to specific intensity (hereafter just "intensity") following Kleint et al. (2016) and

---

[10] The terminology "in emission" or "in absorption" means that the Balmer continuum flux is, respectively, greater than or less than a blackbody curve extrapolation from a fit to continuum windows at $\lambda > 4000$ Å.

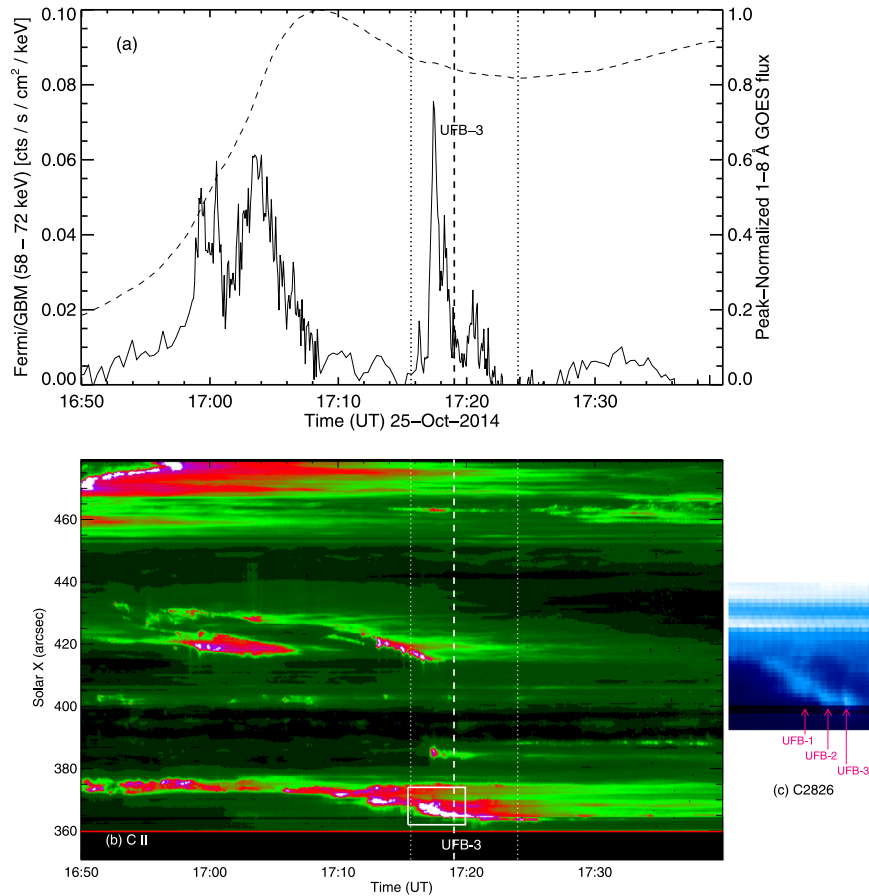[11] Often used to indicate the atmospheric depth.

Figure 1. (a) *Fermi*/GBM hard X-ray light curve (solid curve; from detector n4) and *GOES* soft X-ray light curve (dashed) of the X1 flare with *GOES* peak at 17:08. The fourth major impulsive peak (indicated by vertical dotted lines) occurs at 17:17. The vertical dashed line indicates the time of UFB-3 at 17:19 (see the text). (b) Evolution of the C II line-integrated intensity (linear scaling without continuum or pre-flare subtraction) from the *IRIS* FUV spectra. The vertical lines are the same as in panel (a). The red horizontal line indicates the positions below where there are no *IRIS* data. (c) NUV continuum intensity measure C2826 over a shorter time interval (17:15:27–17:19:55; x-axis) and smaller spatial extent along the slit (solar X from 362″ to 374″), corresponding to the boxed region in panel (b). The umbral flare brightenings are indicated as UFB-1, UFB-2, and UFB-3, and the intensity scaling is logarithmic. The horizontal dark line is the fiducial mark.

Kowalski et al. ([2017a](#)) by using the time-dependent effective area curves (Wülser et al. [2018](#)). By comparing the fiducial marks in the far-UV (FUV) and NUV data, we found that a (downward) shift by one pixel in the FUV spectra was necessary to align them with the NUV spectra. We found that a shift of -0.16 Å was required to calibrate the velocity (using the Ni 2799.474 Å line, as suggested by *IRIS* Technical Note 26) in the level 2 data that we used for our analysis. We note that more recently calibrated data do not require such a shift, since the whole *IRIS* archive was reprocessed in 2017/2018 including an improved wavelength calibration. In general, it is always best to check the calibration of the wavelength using the instructions provided in *IRIS* Technical Note 26.

Usually, to strike the best balance between cadence and data rate, only narrow wavelength regions around specific lines of interest are read out from *IRIS*. Instead, we obtained the observations with a custom observing mode that downlinked the full spectral range of *IRIS* with two-pixel binning in the dispersion direction ($\lambda = 1331.69$–1358.04 Å and $\lambda = 1389.52$–1406.41 Å at 0.0256 Å pixel^{-1} in the FUV and $\lambda = 2783.93$–2834.95 Å at 0.051 Å pixel^{-1} in the NUV) and binning by two in the spatial direction (thus, $0''33$ binned-pixel^{-1} corresponding to ∼250 km binned-pixel^{-1} at the distance of the Sun). The full *IRIS* spectral range was used for a robust identification and characterization of

the FUV and NUV continua in flares; with limited wavelength ranges of typical *IRIS* readout modes ("linelists"), it is not always possible to accurately determine the continuum intensity due to multiple broad, asymmetric flares lines of Mg II, Fe II and other species. The NUV spectral range of *IRIS* (hereafter *IRIS* NUV) has a relatively line-free continuum region at $\lambda \sim 2826$ Å that has been useful as a proxy of the Balmer continuum component of the white-light radiation for comparisons to the predictions of electron beam heating models (Heinzel & Kleint [2014](#); Kleint et al. [2016](#); Kowalski et al. [2017a](#)). In this paper, we calculate this quantity and compare to the continuum level over the entire spectral range of *IRIS*.

2.2. Fermi/GBM X-Ray Data

The *Fermi*/GBM (Meegan et al. [2009](#)) provides high time resolution (4 s, or 1 s in burst mode) X-ray data of solar flares from 8 keV to 40 MeV. *RHESSI* observed the main peak of the flare, but the imagery indicates that the loop-top source dominated the 25–50 keV emission, and *RHESSI* also suffered from significant pileup (Kleint et al. [2017](#)). We use the *Fermi*/GBM data late in the flare when pileup was not significant in several of the least sunward facing detectors.

The *Fermi*/GBM has two types of scintillation detectors: twelve NaI detectors that are sensitive at $E \lesssim 200$ keV and two

bismuth germanate detectors that are sensitive at $E \gtrsim 200$ keV. For spectral analysis (Section 4.2), we use data from detector NaI_n0 (hereafter "n0"), which is the third most sunward-facing detector and does not suffer from pile-up effects[12] over the time of the decay phase of this flare. For light curve analysis, we also use data from detectors NaI_n4 and NaI_n5 (hereafter "n4" and "n5" respectively), which are more sunward-facing in the early rise phase of the flare. The Solar Soft (SSW) IDL OSPEX is used to retrieve and analyze the *Fermi*/GBM data. First, we retrieve a detector response (rsp2) file for the time interval of 16:35–17:36. The background is chosen before and after the X1 event (during *Fermi* night) in the time intervals of 16:15–16:35 and 17:50–18:05. Since the detector angles relative to the Sun change over the first few minutes of this flare,[13] we divide the OSPEX count rate by the cosine of the angle between the detector normal and the Sun.

2.3. Overview of the Flare

The *Fermi*/GBM data from detector n4 at hard X-ray energies, $E = 58$–72 keV, are shown in Figure 1(a), and the light curve exhibits four main hard X-ray peaks at 16:59:17, 17:00:23, 17:03:31, and 17:17:27 with comparable amplitudes.[14] Also shown are the soft X-rays (1–8 Å) from *GOES*.[15]

The SOL2014-10-25T17:08:00 flare was a three-ribbon flare with two ribbons in the sunspot plage and a third ribbon crossing two umbrae within a triple-umbral complex (Bamba et al. 2017). The X1 flare was the largest and the last of three flares that were triggered by an intruding positive polarity to the east of the main polarity inversion line, in accord with the triggering mechanism of Kusano et al. (2012). Following the nomenclature for the ribbons used in Bamba et al. (2017), the XR3 ribbon develops into the umbrae and crosses the *IRIS* slit during the decay phase of the fourth *Fermi*/GBM hard X-ray peak in Figure 1(a). The XR3 ribbon is seen in Figure 2, where we show three context images at 17:19: panel (a) shows the *SDO*/Atmospheric Imaging Assembly (AIA; Lemen et al. 2012) 1700 image with the *IRIS* field of view indicated, panel (b) shows an *IRIS* SJI C II image, and panel (c) is the *IRIS* SJI 2832 image. The XR3 ribbon is very faint in SJI 2832, but the contrast against the umbral intensity is large. Li et al. (2019) found Fe XXI emission blueshifted by 143 km s^{-1} in the *IRIS*/FUV spectra of the XR3 ribbon. The high-temperature, low-density plasma is not analyzed further here. A comparison of flare intensity in the *IRIS* NUV spectra and SJI 2832 images for the X1 flare has been discussed in Kleint et al. (2017), who found that the relative contribution of Balmer continuum emission to the SJI 2832 radiation is nearly 70% during the times when the XR3 ribbon crosses the slit (see the middle panels of their Figure 6). In this paper, we present a detailed analysis of the *IRIS* spectra of the umbral flare ribbon XR3.

---

[12] NaI_n05 is the most sunward-facing detector and suffers from obvious pileup at the peak of the hard X-ray.

[13] The NaI_n0 detector changes from the least sunward-facing orientation to the third most sunward-facing orientation from 17:01 to 17:05, which affects the rise phase of the hard X-rays.

[14] The main peak at 17:04 may suffer from some pileup, thus making the 58–72 keV light curve an upper limit on the flux during this peak.

[15] Bamba et al. (2017) claim there is an error in the time registry for these *GOES* data, but we do not see evidence to support this.

3. A New Diagnostic for Deep Atmospheric Heating

3.1. Identification of NUV Continuum Flare Kernels

In this section, we present the C II ribbon development and describe how we identify the largest NUV continuum enhancements, which occur in the late phase when the XR3 ribbon develops into an umbra. The large contrast of the flare ribbons in umbrae (which are rather unusual environments for flare ribbon development) provides more robust comparisons to RHD models than flare spectra with low intensity contrast in the plage regions, which vary significantly due to the granulation evolution.

The flare ribbons crossed the slit at many times and locations in the 2014 October 25 X1 flare. The intensity integrated over each C II line from -60 to $+90$ km s^{-1} is shown in Figure 1(b) and readily indicates the times when, and locations where, the XR1, XR2, and XR3 flare ribbons cross the *IRIS* slit. However, the detailed formation of C II in flares has yet to be investigated for a range of heating levels outside of quiet-Sun conditions (Rathore & Carlsson 2015). Since C II has previously been analyzed extensively in *IRIS* data of solar flares (e.g., Tian et al. 2015; Sadykov et al. 2016), and they provide a comprehensive, high-contrast overview of the flaring ribbon evolution, we show their line-integrated evolution here but do not return to a detailed analysis of these lines in this paper.

We identify candidate NUV continuum enhancements (and, by proxy, white-light-emitting kernels) with a running difference of the line center intensity of Fe II at $\lambda = 2814.45$ Å, which we expect to brighten with the NUV continuum due to their similar formation conditions in flares (Kowalski et al. 2017a). Detailed justification for using Fe II to find candidate continuum enhancements is given in Appendix A. The time evolution of the NUV continuum region from $\lambda = 2824.5$ to 2825.9 Å is shown in Figure 1(c) over a limited time range. Following Kowalski et al. (2017a), we calculate the average intensity in this wavelength window as C2826;[16] the XR3 flare ribbon in C2826 crosses the *IRIS* slit and sunspot umbra from 17:17 to 17:19 UT in Figure 1(c) and is further evident in SJI 2832 in Figure 2(c). Subtracting the preflare intensity gives the "excess C2826," hereafter C2826′ (following the "prime" terminology for flare-only flux in Kowalski et al. 2012, 2019), and dividing by the pre-flare values gives the "C2826 enhancement" (following the terminology in Kowalski et al. 2015a).

The largest values of the C2826′ (intensity) and the C2826 enhancement occur in the sunspot umbra at $(x, y) = (364\rlap{.}''8, -318\rlap{.}''4)$ at 17:18:24 and 17:19:02 UT during the decay of the fourth hard X-ray event which peaks at 17:17:30. Hereafter, we refer to the brightest flaring pixels in the umbra during this hard X-ray event as the "umbral flare brightenings" (UFBs). The time of UFB-3 is indicated in Figure 1(a) for reference. The peak of UFB-1 occurs at 17:17:31 at the spatial location of $(x, y = 365.8, -318.4)''$. The peaks of UFB-2 at 17:18:24 and UFB-3 at 17:19:02 UT occur in nearly the same location at $(x, y = 364.8, -318.4)''$. However, UFB-2 appears to be less than one pixel to the west (in the positive x direction) of UFB-3, and the apparent motion of the ribbon eastward along the slit is evident from the time of UFB-1 to the time of UFB-3 (see Figure 1(c)). Hereafter, we focus our analysis on the spectra of

---

[16] The value of C2826 was defined as the average intensity from $\lambda = 2825.6$ to 2825.9 Å in the 2014 March 29 spectra in Kowalski et al. (2017a). In this study, we extend the blue end of the wavelength window for C2826 to 2824.5 Å, which is line-free in the 2014 October 25 flare.
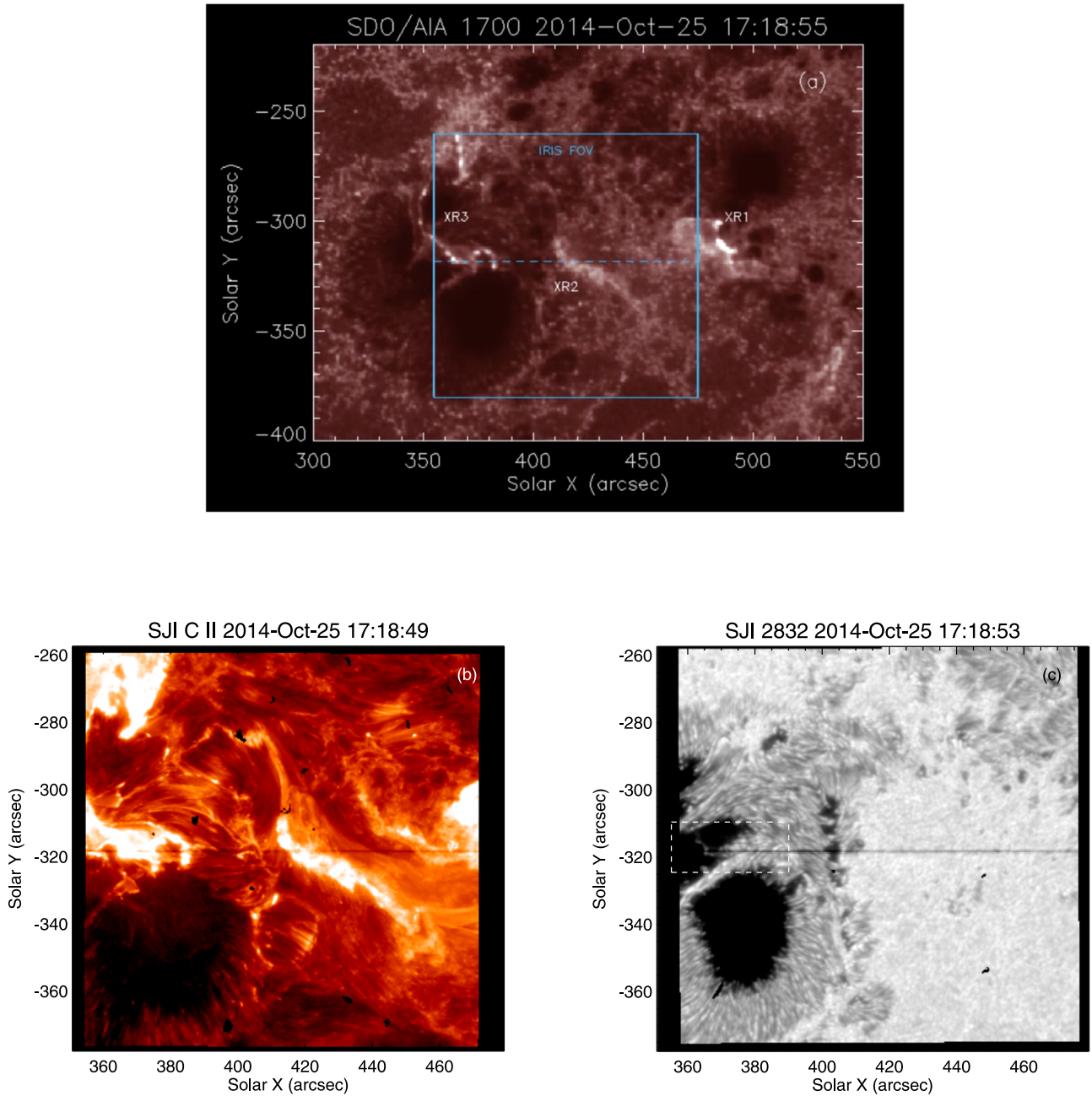
Figure 2. *IRIS* slit context images of the flare ribbons at late times in the 2014 October 24 X1 flare at three different wavelengths. (a) *SDO*/AIA 1700 image (linear intensity scaling) with the XR1, XR2, XR3 ribbons labeled following the nomenclature in Bamba et al. (2017). The *IRIS* slit is indicated as a horizontal dashed line. (b) *IRIS* slit jaw image in the FUV (C II) with a logarithmic intensity scaling. (c) *IRIS* slit jaw image in the Mg II h wing (SJI 2832) with a logarithmic intensity scaling. The box indicates the field-of-view over which the area is calculated in Section 4.1. The XR3 ribbon crossing the *IRIS* slit in the umbra at solar $x \sim 365''$ is apparent at this time (at the onset of the rise phase of UFB-3; see the text) in all images.

UFB-2 and UFB-3, which produced the largest and fastest NUV continuum enhancements in the *IRIS* spectra.

3.2. Continuum Properties of the Umbral Flare Brightenings

The time evolution of C2826 averaged over three spatial pixels (the spatially averaged intensity, $\langle I_\lambda \rangle$) centered at $(x, y) = (364''.8, -318''.4)$ is shown in Figure 3. The UFB-2 and UFB-3 events correspond to the first and second C2826 peaks, respectively. The C2826 enhancement remarkably exceeds the pre-flare umbral intensity by a factor of ten. The $E = 58$–72 keV X-ray light curve

is overplotted in Figure 3, and UFB-3 occurs when the ribbons cross the slit in the decay phase of this hard X-ray peak. From the range of calculated FWHM values of the C2826′ light curve of UFB-3, we constrain upper limits on the duration of heating to $\Delta t_{burst} = 12$–22 s over a solid angle of $0''.33$ (slit width) $\times$ ($0''.40$; NUV spatial resolution), or an area of $\sim 6.5 \times 10^{14}$ cm^2. However, the data do not exclude shorter heating durations over smaller areas. Furthermore, the rise phase of UFB-3 is unresolved since it consists of one temporal point. However, we note 10–20 s is generally the timescale range for soft X-ray derivative bursts characterized in another flare (Rubio da Costa et al. 2016).
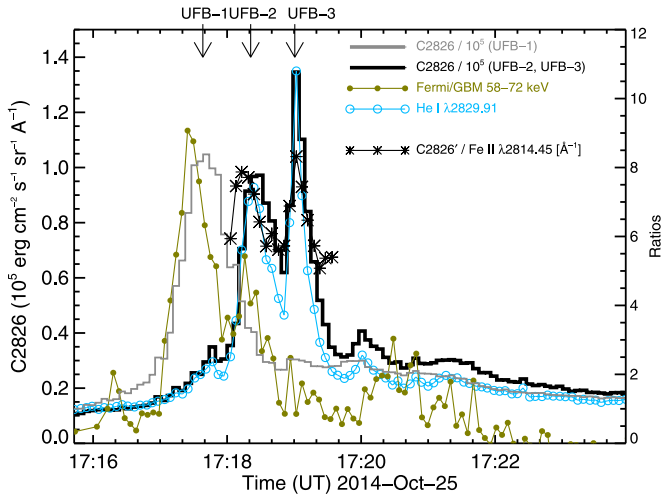
Figure 3. C2826 light curve of UFB-2 and UFB-3 at $(x, y) = (364.8, -318.4)$ arcsec during the fourth major hard X-ray peak, over the same time range as indicated by the vertical dotted lines in Figures 1(a), (b). The peaks of UFB-2 and UFB-3 are delayed with respect to the peak of the hard X-rays in *Fermi*/GBM (olive) because the *Fermi*/GBM is not spatially resolved at the Sun and the ribbons cross the *IRIS* slit at this spatial location at a later time. The continuum-to-line ratios (C2826′/Fe II λ2814.45; asterisks, right axis) exhibit very large values of $\sim$7–8 in the impulsive phases (from 17:18:03 to 17:19:34) of UFB-2 and UFB-3. The light curve of C2826 at the spatial location of UFB-1 is shown in a lighter gray tone; UFB-1 reaches its maximum closer in time to the hard X-ray peak.

Several heating episodes may occur (at least partially) in the same location (e.g., UFB-2 and UFB-3), but this cannot be quantified in any detail even with the impressive spatial resolution of *IRIS* since the ribbons move along the slit from the time of UFB-1 to the time of UFB-3.

The *IRIS* NUV spectrum at the peak of UFB-3 is shown in Figure 4(a). This spectrum exhibits the most robust characterization of the *IRIS* NUV continuum to date during a solar flare. The flare spectrum shows that the NUV continuum intensity level extrapolated (over the horizontal red line) from C2826′ extends over a spectral range of $\Delta \lambda = 50$ Å. The horizontal line extrapolation provides an estimate for the relative, wavelength-integrated continuum energy in the NUV spectral range of *IRIS*. We find that only $\sim$25% of the UFB-3 peak flare kernel brightness in the *IRIS* NUV spectral range is attributed to the continuum radiation, while the majority of the wavelength-integrated kernel brightness (nearly 70%) is due to the Mg II lines.

The C2826′ intensity from *IRIS* during other flares has been used to compare directly to radiative–hydrodynamic flare models (Heinzel & Kleint 2014; Kleint et al. 2016; Kowalski et al. 2017a). But are the C2826′ ribbons in the 2014 October 25 X1 flare spatially resolved for a direct comparison of the value of C2826′ ($\langle I'_\lambda \rangle \approx 1$–$1.5 \times 10^5$ erg s^{-1} cm^{-2} sr^{-1} Å^{-1}; Figure 3) to model snapshots? We use the *iris_sg_deconvolve.pro* routine to deconvolve the UFB-1 and UFB-3 peak spectra by the *IRIS* point-spread function as described in Courrier et al. (2018). We find that after 15 iterations of the deconvolution procedure, the NUV spectra increase in brightness by factors of 1.2–2. The *IRIS* NUV resolution is 0″.4 or 1.2 (binned) pixels, and the spatial FWHMs of UFB-1, UFB-2, and UFB-3[17] are 3–6 pixels, corresponding to 700–1400 km at the Sun; in Figure 1(c), it is

---

[17] UFB-3 occurs adjacent to a fiducial mark in the spectra (Figure 1(b)), and we are unable to quantify the full spatial extent of the kernel.
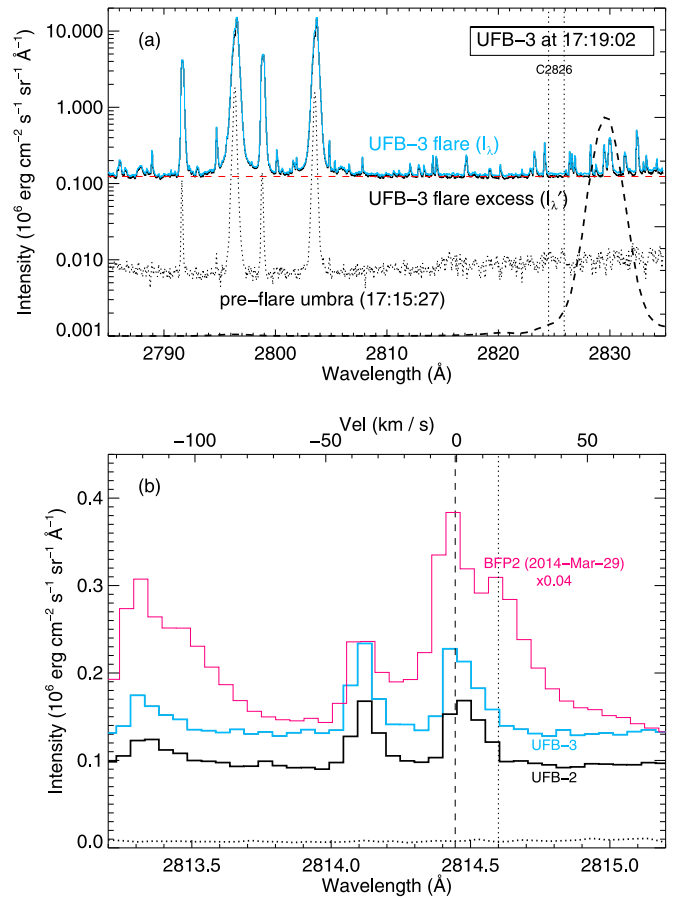

Figure 4. (a) *IRIS* NUV spectra of the brightest peak of the umbral flare brightening light curve in Figure 3. The spectra were averaged over three pixels (1″) in the spatial dimension. Vertical dotted lines show the extent of the line-free continuum region C2826. The horizontal red dashed line indicates the value of C2826′ extrapolated over the full spectral range of the *IRIS* NUV; C2826′ adequately represents the NUV continuum flare excess intensity over this range. The effective area curve for the *IRIS* slit jaw SJI 2832 is shown as a dashed curve for reference. (b) The Fe II λ2814.45 lines in the UFB-2 (black) and UFB-3 (light blue) spectra indicate asymmetries at redder wavelengths than the rest wavelength, which is indicated by the vertical dashed line. The redmost extent of the Fe II λ2814.45 line in UFB-2 and UFB-3 is indicated by a vertical dotted line. The other flare emission lines in panel (b) are Fe II at $\lambda = 2813.322$ Å and Fe I at $\lambda = 2814.115$ Å. The umbral flare brightening profiles are compared to the spectra (scaled by 0.04; see Section 5) of the bright flare footpoint ("BFP2"; Kowalski et al. 2017a) in the X1 flare on 2014 March 29. The 2014 March 29 flare data have been binned to the same spectral binning as the 2014 October 25 flare data and are shown averaged over three pixels in the spatial direction. The red-wing asymmetry in the 2014 March 29 flare is broader, brighter, and redder; it is also clearly spectrally resolved when this binning is not applied.

apparent that the NUV continuum radiation (C2826) from the UFBs is bright over a few pixels only. In higher-resolution Hα data of umbral flare ribbons, very narrow widths of $\sim$100 km are observed (Sharykin & Kosovichev 2014), which suggests there may be significant unresolved structure in our *IRIS* observations. Higher-quality observations (i.e., without saturation) of the widths and motions of plage and umbral kernels will be important to obtain with the Daniel K. Inouye Solar Telescope at very high time resolution.

3.3. The Fe II 2814.45 Å Line in Umbral Flare Brightenings

The Fe II λ2814.45 emission line has been recently studied using radiative–hydrodynamic models of flares (Kowalski et al. 2017a)

and has revealed two emission line components: a line component centered near the rest wavelength and a spectrally resolved, broad emission component to the red of the rest wavelength. Compared to other chromospheric flare lines, the Fe II $\lambda2814.45$ line exhibits one of the lowest opacities, and the optical depth does not build up as fast in that line as in the Balmer lines or in Mg II. Thus, the properties of Fe II $\lambda2814.45$ constrain the dynamics in deep layers of the flaring chromospheric condensation and stationary flare layers below (Kowalski et al. 2017a), where the white light and *IRIS* NUV continuum radiation may originate. The similar temperature and density dependencies of Fe II $\lambda2814.45$ and hydrogen Balmer bound–free radiation are shown in Appendix A.

In Figure 4(b), we show an inset of several flare emission lines around the region of the Fe II $\lambda2814.45$ line in UFB-2 and UFB-3. We measure the bisector at 30% maximum for the Fe II $\lambda2814.45$ Å emission line to be $+3.7 \pm 2.9 \, \mathrm{km \, s^{-1}}$. This is just greater than a 1σ redshift detection.[18] However, the line profile shape exhibits asymmetric brightening at $\lambda > \lambda_{\mathrm{rest}}$ such that there are more spectral bins with an intensity greater than or equal to the line half-maximum on the red side than on the blue side. We show vertical dashed lines at λ_{rest} and vertical dotted lines at $\lambda - \lambda_{\mathrm{rest}} = +16 \, \mathrm{km \, s^{-1}}$ to indicate the red extent of this profile asymmetry. The Fe II at $\lambda = 2813.32$ Å line exhibits a similar asymmetric profile and redshift ($4.5 \, \mathrm{km \, s^{-1}}$) to the Fe II at $\lambda = 2814.45$ Å line, while the Fe I $\lambda = 2814.115$ Å line exhibits no evidence of a redshift or an asymmetric profile. Furthermore, UFB-2 and other flare spectra show similarly redshifted and asymmetric Fe II $\lambda2814.45$ profiles to UFB-3. These three lines are of particular utility for studying flares, as they fall within a standard window common to the *IRIS* NUV linelists, and thus provide the opportunity to compare with a large archive of observations. With full spectral readout, there are numerous additional Fe II and Cr II lines with similar profiles available, as discussed in Section 4.3 and Appendix B. The asymmetric, redshifted profiles of these Fe II lines and other emission lines can be synthesized from RHD models to constrain the chromospheric velocity field in white-light-emitting layers at high time resolution.

3.4. The Continuum-to-line Ratio in IRIS Spectra

The UFB spectra reveal that the ratio of the NUV continuum radiation to the Fe II line intensity is an interesting diagnostic in flares. This continuum-to-line ratio can be readily obtained from spectra with narrow wavelength coverage; like an equivalent width, it is independent of uncertainties (e.g., Courrier et al. 2018; Wülser et al. 2018) in the absolute intensity calibration. We define the continuum-to-line ratio as the excess C2826 (C2826′) divided by the wavelength-integrated, continuum-subtracted, and preflare-subtracted intensity of the Fe II $\lambda2814.45$ line. The continuum-to-line ratio is hereafter denoted as C2826′/Fe II $\lambda2814.45$ (with units of Å^{-1}). The evolution of this quantity varies between 7 and 8 over the peaks of UFB-2 and UFB-3 and is shown in Figure 3. At the peak of UFB-1 (not shown), the continuum-to-line ratio is also large near 7. Subtracting the last decay phase spectrum of UFB-2 from the peak of UFB-3 at the spatial location of the light curve in Figure 3 gives the newly brightened flare

radiation assuming that UFB-2 and UFB-3 occur at different locations within the spatial resolution. For this spectrum, the value of C2826′/Fe II $\lambda2814.45$ is even larger (≈12). A comparison of the C2826′/Fe II $\lambda2814.45$ ratios among many flares will be presented in E. Butler et al. (2019, in preparation).

The Fe II $\lambda2814.45$ line in the *IRIS* NUV spectrum is an important diagnostic in flares because the line is produced (assuming local thermal equilibrium; LTE) over a similar temperature range of $T \sim 8000$–$18,000 \, \mathrm{K}$ as hydrogen bound–free radiation (Kowalski et al. 2017a, and shown in detail in Appendix A), which contributes to the C2826′ intensity in flares (Heinzel & Kleint 2014). Thus, the ratio of these two quantities reflects the amount of significant heating ($T \gtrsim 8500 \, \mathrm{K}$) in deep layers of the atmosphere that exhibit $\tau_\lambda \lesssim 1$ for continuum radiation and $\tau_\lambda \gtrsim 1$ for Fe II $\lambda2814.45$ radiation. The ratios from optically thin, uniform slabs with low to moderately high densities ($\rho < 10^{-9} \, \mathrm{g \, cm^{-3}}$) at $T \sim 10,000 \, \mathrm{K}$ are $\lesssim 0.8$ (Appendix A), which are far less than the observed values of 7–8 in the UFBs. Radiative–hydrodynamic modeling and the detailed interpretation and analysis of large values of C2826′/Fe II $\lambda2814.45$ in the UFBs are outside the scope of this paper and will be presented in Paper II.

4. Other Observational Properties of the Flare

In order to model the UFBs and the continuum-to-line ratios with electron beam heating simulations in Paper II, several comprehensive input parameters (electron beam energy and power-law index) and other constraints from the emission lines are presented in this section. In Section 4.1, we calculate the flare area from high spatial resolution imagery of the flare ribbons. This flare area is combined with the nonthermal electron power inferred from *Fermi*/GBM data in Section 4.2 to give the energy flux density of beams assumed to heat the lower atmosphere. In Section 4.3 and Appendix B, we discuss properties of the many other Fe II emission lines in the UFBs, as well as species such as Cr II and Fe I, and the constraints they provide on atmospheric models. In Section 4.4, we discuss the properties of a He I emission line in the *IRIS* NUV that will complement the constraints from the Fe II lines.

4.1. Evolution of the Flare Ribbons

High spatial resolution flare area estimates are critical for obtaining an accurate heating rate for modeling the RHD response (Krucker et al. 2011). However, the continuum contrast outside the umbra is low, which causes flare area measurements to be difficult in solar flares for even large flare energies. Generally, the non-flaring photospheric intensity in the NUV Mg II h wing is $50\times$ brighter than the pre-flare umbral NUV intensity, and the large-amplitude, gradual variation from photospheric convection outside of the sunspot makes the identification of bona fide flare continuum enhancements difficult (we refer the reader to Kleint et al. 2017 for some properties of NUV enhancements away from the sunspots).

We present an algorithm that identifies pixels that brighten impulsively in flares. This algorithm excludes gradual evolution of the solar granulation that can be falsely identified as flare kernels, and the method is applicable to other data sets with high time and high spatial resolution. Using the intensity-calibrated SJI 2832 images (with a cadence of 16 s), we set a threshold excess intensity (T.E.I.) value for impulsive pixels in SJI 2832 to $10^5 \, \mathrm{erg \, cm^{-2} \, s^{-1} \, sr^{-1} \, Å^{-1}}$, which corresponds to

---

[18] Adding a systematic uncertainty of $1.8 \, \mathrm{km \, s^{-1}}$ and a statistical uncertainty of $2.3 \, \mathrm{km \, s^{-1}}$ in quadrature.
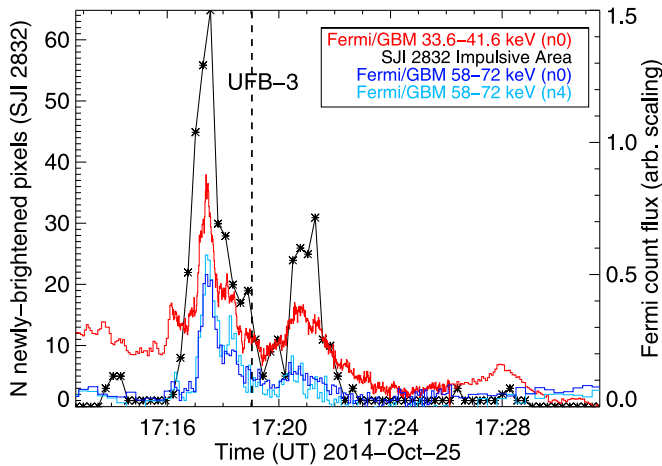
Figure 5. The newly brightened (impulsive) flare area in SJI 2832 and the *Fermi*/GBM hard X-ray light curve during the fourth hard X-ray peak. The conversion from pixels to area for these observations (which employ on-board binning) is 6×10^{14} cm^2/pixel. The UFB-3 occurs during the late phase of the fourth hard X-ray peak, but the evolution of the flare area in SJI 2832 follows the hard X-ray light curves. Note, the newly brightened flare area in SJI 2832 is calculated from the region indicated by the box indicated in panel (c) of Figure 2.

$\sim$30% of the maximum excess intensity observed over the entire observation sequence. We consider here only the umbral region indicated in the SJI 2832 image by the box in Figure 2(c). A pixel at time t in image i is counted as an impulsive flare pixel if the following criteria are met: (1) the excess intensity in this pixel at t is greater than the T.E.I.; (2) the excess intensity in this pixel at $t - 48$ s ($i - 3$) or $t - 64$ s ($i - 4$) is less than $0.5 \times$ T.E.I; and (3) the excess intensity at $t + 160$ s ($i + 10$) is less than $0.5 \times$ T.E.I. These criteria identify newly flaring, impulsive pixels in SJI 2832 by efficiently excluding a significant number of pixels that exhibit a much more gradual evolution with sustained excess values. It is not possible to tell whether these gradual brightenings are due to changes in the granulation or are related to the flare, as in the so-called "type II white-light flare" variations (Matthews et al. 2003; Procházka et al. 2017). Hereafter, we refer to the impulsive flare areas using this algorithm as "newly brightened" flare areas.

The number of newly brightened flare pixels (where each pixel corresponds to an area of 6×10^{14} cm^2 at the Sun) in the umbral region of SJI 2832 is shown as a function of time in Figure 5 and is compared to the *Fermi*/GBM $E = 35$–41 keV and $E = 58$–72 keV light curves. The newly brightened flare area and hard X-ray emissions follow each other closely (see D. Graham et al. 2019, in preparation), which suggests that the heating in these pixels (over a small region in the flare) is related to the nonthermal electrons that produce the fourth hard X-ray peak.[19] In the decay phase of the fourth hard X-ray peak, the newly brightened ribbon areas have decreased as they progress through the umbra. Thus, there are *impulsive* flaring pixels in the *gradual* decay of the hard X-ray peak (which occurs in the gradual decay of a much larger soft X-ray peak). From Figure 5, we obtain a range of newly brightened flare areas to be 7×10^{15} cm^2 (17:19; at the peak UFB-3) to 4×10^{16} cm^2 (17:17:30; at the peak of the fourth hard X-ray peak). This information is combined with constraints from the

Fermi/GBM spectrum in Section 4.2 to infer the energy flux in electron beams.

Whereas the *Fermi*/GBM hard X-rays originate from the entire flaring area, the SJI 2832 data used to calculate the flare area are rather limited in field of view (see Figure 2(c)). Thus, we use our algorithm[20] to calculate the newly brightened flare area in *SDO*/1700, which provides a complete field-of-view characterization of the flare region but with lower spatial resolution. The newly brightened flare area from *SDO*/1700 is $\sim$2 $\times 10^{17}$ cm^2 at the time of the peak of the fourth hard X-ray light curve, and it falls to $\sim$5 $\times 10^{16}$ cm^2 at the times of the (spectral) UFBs. These areas are 10–40$\times$ larger than obtained from the umbral region in SJI 2832. Note that several bright kernels in the *SDO* images are saturated during the flare, making the areas from *SDO*/1700 overestimates of the true flaring area at some times.

We also investigate whether the bright flare sources that cross the *IRIS* slit (UFB-1, UFB-2, or UFB-3) are obviously brighter than other newly brightened flare pixels in the SJI 2832 images within the box indicated in Figure 2(c). Many of the brightest SJI 2832 pixels occur near the maximum of the hard X-ray light curve in Figure 5. To determine how the UFBs from the spectra compare to the brightest flare excess pixels that do not cross the slit, we fold the *IRIS* spectra at the peaks of UFB-2 and UFB-3 with the effective area curve of SJI 2832 (Figure 4) to produce the synthetic values of SJI 2832; the synthetic excess intensity values[21] are 1.7×10^5 and 2.3×10^5 erg cm^{-2} s^{-1} sr^{-1} Å^{-1} for UFB-2 and UFB-3, respectively, while the brightest SJI 2832 excess value is 3.5×10^5 erg cm^{-2} s^{-1} sr^{-1} Å^{-1}. There are 117 pixels (or 23% of the pixels brighter than the T.E.I.) in the SJI 2832 images that become as bright as or brighter than the UFB-2 spectrum, and there are 35 (or 7% of the pixels brighter than the T.E.I.) greater than or equal to the brightness of UFB-3. Clearly, a significant number of pixels that do not intersect the *IRIS* slit are brighter than the synthesized SJI 2832 values from the UFB-2 and UFB-3 spectra, suggesting that the continuum brightness of the umbral flare brightenings (UFB-2 and UFB-3) that cross the *IRIS* slit are not uniquely large.

4.2. Fermi/GBM Spectral Analysis

The hard X-rays from *Fermi*/GBM indicate the presence of nonthermal electrons in the flare, which are thought to produce the heating responsible for the white light (e.g., C2826) increase. To determine if nonthermal electrons (as constrained from *Fermi*) are sufficient to explain the *IRIS* spectra, we infer the properties of a nonthermal electron beam using the standard thick-target formulae. The nonthermal electron distribution is parameterized by a power-law index (δ), an energy flux density (given by $a \times 10^x$ erg cm^{-2} s^{-1}; hereafter, abbreviated by aFx), and a low-energy cutoff (E_c) of the distribution, which is almost always an upper limit. Following the thick-target modeling of Milligan et al. (2014), we fit the *Fermi*/GBM spectrum at $E = 10$–60 keV with a sum of thick target bremsstrahlung emission, an albedo correction from Compton scattering off the photosphere (Kontar et al. 2006), and a

---

[19] This also shows that the fourth hard X-ray peak in *Fermi*/GBM is a result of the X1 flare ribbons and not due to a particle event with a non-solar origin.

[20] To calculate newly brightened emission in *SDO*/AIA 1700 at time t we used running differences of $t - 24$ s, $t - 48$ s, and $t + 168$ s, and we added the number of pixels that were below 50% of a high threshold value, which we took to be 30% of the saturation ($\sim$15,000 counts).

[21] The synthetic SJI 2832 intensity values from the UFB spectra are not averaged over three spatial pixels in this analysis.
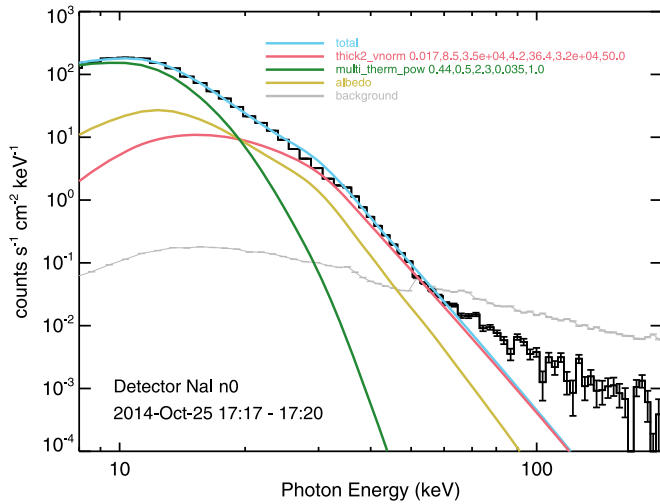
Figure 6. Multi-component fit to the $E = 10$–60 keV *Fermi*/GBM (NaI n0 detector) spectrum from 17:17–17:20 with therm_multi_pow + albedo + thick2_vnorm ("total"). Parameters as returned by OSPEX for each component are given in the legend. Fitting during times and using other methods of background subtraction give similar parameters. Note that the $\sim$20–40 keV energy range is excluded from the fit due to known calibration issues with *Fermi*/GBM.

multi-thermal power-law spectrum. The fits were done using the SolarSoft OSPEX software in IDL and are shown in Figure 6 for the time-interval 17:17–17:20 (indicated by vertical dotted lines in Figure 3). Varying the fit interval to two minutes within this window gives similar results. We fit all energy intervals at $E = 10$–60 keV using the same background times. Because it is known that there is an iodine k-edge (at 33 keV) in the detector (Meegan et al. 2009), which causes spectral fitting from 20–40 keV to be problematic, we also fit only $E = 40$–60 keV with a thick target model but find a similar power law. We conclude that the hard X-rays are consistent with a thick-target electron spectrum that has a power-law index of $\delta = 8$–9 and an upper limit to the low-energy cutoff of 35–40 keV. Note that the Compton scattering and photoelectric absorption of outgoing hard X-ray photons from the heated chromosphere have not been taken into account in the X-ray spectral fits, whereas a limb observation has shown that the hard X-ray source (in another flare) is low enough to make the Compton opacity significant (Martínez Oliveros et al. 2012). The extinction of hard X-rays in the evolved atmosphere will be considered in the radiative–hydrodynamic flare model atmospheres in Paper II.

At $E \gtrsim 60$ keV there is clearly a break in the spectrum in Figure 6. While there is a transient burst of hard X-ray and gamma-ray photons at $E \gtrsim 100$ keV to $E \sim 10$ MeV which corresponds to the evolution of the C2826 light curve in Figure 3, this gamma-ray event cannot be constrained to originate from the Sun since *Fermi* was approaching the South Atlantic Anomaly at these times. Thus, the break is likely due to variable background radiation.

The last input parameter for RHD modeling is an estimate of the energy flux density (aFx) of accelerated electrons. Using the fits in Figure 6, we obtain a nonthermal power of 8×10^{27} erg s^{-1}, which is an average over the time interval. A fit to the times of the fourth HXR peak at 17:17:20–17:17:40 gives a power of 10^{28} erg s^{-1} (with similar cutoff and power-law indices). The hard X-ray count rate at the time of UFB-3 is $\sim 1/10$ of the max count rate in the fourth peak (see

Figures 1(a) and 5), which allows us to estimate that the nonthermal electron power is 10^{27} erg s^{-1} at the time of the UFBs in the *IRIS* spectra. The area estimated in Section 4.1 from *SDO*/1700 gives a flux density estimate of 2×10^{10} erg cm^{-2} s^{-1}, while the area from SJI 2832 gives 1.5×10^{11} erg cm^{-2} s^{-1}. We thus obtain a range of 2F10 $-$2F11 for the nonthermal electron energy flux density for input to RADYN modeling.

The power-law index of the hard X-ray emission is very soft at these late times in the flare. The analysis of *RHESSI* data for this flare also indicates a large power-law index at earlier times (Kleint et al. 2017). The *RHESSI* imagery suggests the hard X-ray (25–50 keV) source is coronal, which may be due to a thick-target nonthermal coronal source or due to pileup of low-energy photons from a thermal coronal source. Because *Fermi*/GBM is spatially unresolved, we cannot rule out that the $E \gtrsim 40$ keV emission originates from a thick target coronal source (Veronig & Brown 2004), but we have ensured that we use data from the detectors of *Fermi* that do not suffer from pileup of lower-energy photons. We note that Thalmann et al. (2015) used *RHESSI* data of other flares from AR 12192 and found very soft electron spectra of $\delta \sim 9$ in the decay phase and very large nonthermal electron energies as well. There are many other examples of soft power-law indices in flares in Solar Cycle 24 (Milligan et al. 2014; Kerr et al. 2015; Thalmann et al. 2015; Warmuth & Mann 2016).

4.3. Other Emission Line Properties of the Umbral Flare Brightenings

The full spectral readout employed for these data allow a unique and comprehensive identification of flare emission lines in the *IRIS* NUV wavelength range. There are many lines of Fe II in the flare spectrum in Figure 4, as well as for other species, and multiple lines from the same species provide powerful capability to disambiguate blends. A number of line identifications in the flaring NUV spectrum are shown in Figures 7 and 8, and a full list of identifications and intensities ($\langle I_\lambda \rangle$) at the peak of UFB-3 are given in Appendix B. While the strongest lines are those of Mg II, there are numerous strong lines of Fe II, Cr II, Fe I, and other species, for which ratios of intensity among emission lines (e.g., Fe II $\lambda 2814.45/\lambda 2832.39$) can also provide valuable constraints on models.

Another valuable capability provided by the full spectral range of these data is to characterize the contributions to SJI 2832 images in detail. The spectral range from Figure 4 at the peak of UFB-3 is enlarged in Figure 7 to show the line and continuum contributions. The brightest emission lines in the SJI 2832 bandpass are: Fe II $\lambda 2826.58$, $\lambda 2826.86$, $\lambda 2828.26$, $\lambda 2828.73$, $\lambda 2829.46$, $\lambda 2831.75$, and $\lambda 2832.39$; He I $\lambda 2829.91$ (see Section 4.4); Cr II $\lambda 2831.30$ and $\lambda 2833.29$; Fe I $\lambda 2826.39$; and Ti II $\lambda 2833.015$. Accurate SJI 2832 predictions from RHD models of flares need to include the contribution from these lines in addition to the continuum radiation. We calculate the filter-weighted specific intensity (Sirianni et al. 2005) from the spectrum with the SJI effective area curve. This calculation indicates that $\sim$60% of the flaring SJI 2832 count rate is due to the NUV flare continuum radiation, which is consistent with the findings of Kleint et al. (2017) for these data. In Figures 7 and 8, we show the estimated C2826′ continuum level lowered by 5%, which seems to slightly better represent the continuum intensity between emission lines at $\lambda \lesssim 2823$ Å.
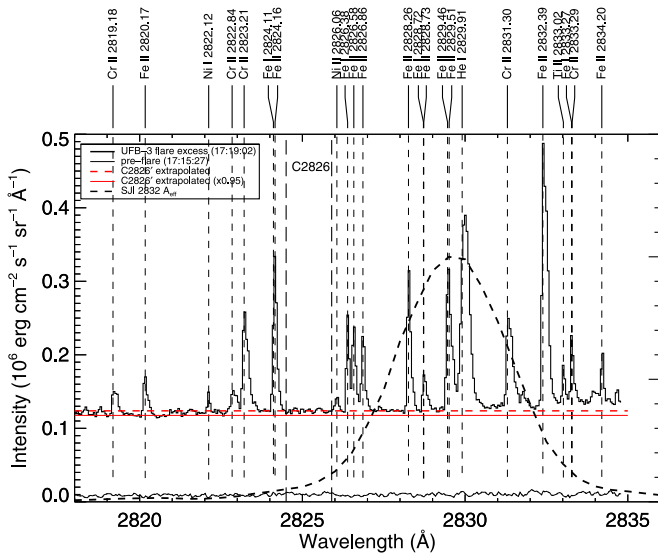
Figure 7. Enlarged view of the UFB-3 peak flare spectrum over the wavelength range of SJI 2832. Many Fe II and Cr II lines exhibit similar profile asymmetries, and the He I 2829.91 Å line is redshifted and broad. We adjust the value of C2826′ by 5% to show that it better represents the excess NUV continuum intensity at $\lambda \lesssim 2823$ Å.
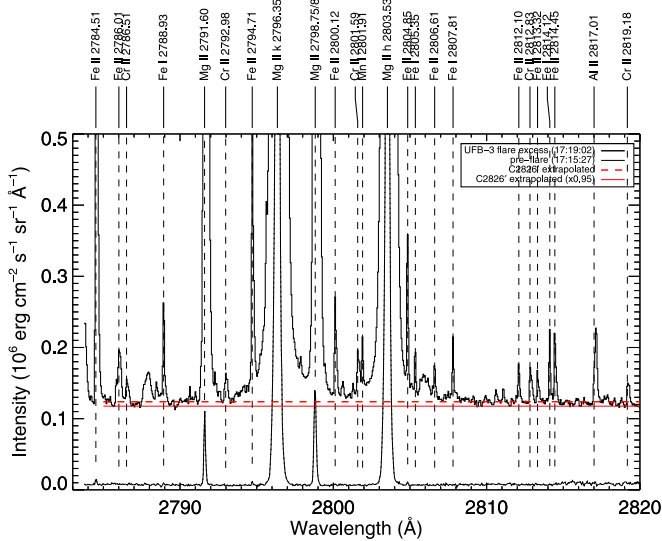

Figure 8. Some line identifications of the brighter lines in the UFB-3 peak flare spectrum at shorter NUV wavelengths around Mg II. We adjust the value of C2826′ by 5% to show that it better represents the excess NUV continuum intensity at $\lambda \lesssim 2823$ Å.

A number of lines in the UFB-3 peak excess intensity spectrum are identified and discussed further in Appendix B. Briefly, rest wavelengths for Fe II, Cr II, and Fe I are adopted primarily from Nave & Johansson (2013), Sansonetti & Nave (2014), and Nave et al. (1994), respectively, with additional data on wavelengths and A-values obtained from the NIST (Kramida et al. 2018), Kurucz (2018), and R. L. Kelly (https://www.cfa.harvard.edu/ampcgi/kelly.pl) databases and references therein. Identifications were verified by: (1) comparing line positions and profiles to those from the same species, and (2) comparing intensities from LTE calculations at different temperatures to the observed intensity ratios for each species, with opacity considered as discussed below. In Appendix B, we give measured wavelengths in this flare

spectrum using 30% bisectors. Most bisector values for Fe II, Cr II, and Mg II are systematically redshifted by an amount greater than or approximately equal to the Fe II λ2814.45 line discussed in Section 4.3.

Nineteen Fe II line profiles, comprising 24 of the 31 Fe II lines listed in Appendix B, are shown for the UFB-3 peak in Figure 9. These are reasonably strong, isolated features with either no evidence of significant blends from other species, or minor blends that can be accounted for, since multiple other lines are observed from those species to constrain any impact the blends would have. This provides many ratios between Fe II line intensities that can be used to constrain model atmospheres. Compared to the ratios in the flare, the LTE intensity ratios are systematically over-predicted for the strong Fe II lines. We speculate that optical depth in the brighter Fe II prevents a relatively larger amount of emission from escaping from the stationary flare layers (below the chromospheric condensation; see Kowalski et al. 2017a) in these lines. This speculation is supported by the fact that for the two brightest Fe II lines, λ2784.512 and λ2832.394, the rest component is less pronounced relative to the red wing than it is for the weaker Fe II lines. These two Fe II lines also exhibit the largest 30% bisectors (7–8 km s^{-1}) among all Fe II line bisectors (-1 to $+8$ km s^{-1}; see Appendix B) that are reliably measured. This evidence for optical depth attenuation from the Fe II line ratios and profiles is consistent with the evidence from the continuum-to-line ratio (Appendix A, Section 3.4, Paper II). Detailed examination of this hypothesis can be done by simulating all the observed Fe II lines and lines of other species as discussed further in Appendix B.

4.4. A New Flare Emission Line: He I λ2829.91

We noticed an emission line in the SJI 2832 bandpass that is broader than other lines in this wavelength range. This "line" is the closely spaced He I λ2829.91 Å multiplet, which has been previously identified in the laboratory (Drake 2006; Kramida et al. 2018) and in absorption in the spectra of hot (O- and B-type) stars (Dufton & McKeith 1980; Fahey 1984). This transition results from a high-lying upper level in He I compared to several other important He I flare emission lines (Figure 10). The peak of the profile in the UFB-3 spectrum is redshifted, as for the Mg II lines. The He I profile has comparable broadening to Mg II λ2791.6, but it exhibits a larger 30% bisector velocity ($+11$ km s^{-1}) than Mg II λ2791.6 ($+8$ km s^{-1}) and Fe II λ2814.45 ($+4$ km s^{-1}). The width of the profile is much larger than the instrumental resolution (De Pontieu et al. 2014), which is readily apparent by comparing to the narrower Fe I and Fe II lines. Adding the instrumental and thermal widths in quadrature, we find that the width of He I λ2829.91 equates to a thermal broadening corresponding to $T \sim 75{,}000$ K, which is much larger than expected for a neutral helium line. The large FWHM (0.28 Å) of the He I 2829.91 Å line and the widths of the Mg II lines are likely due to a nonthermal broadening mechanism, such as a large optical depth and/or a spectrally unresolved redshifted component. The larger bisector velocity than Mg II 2791.6 Å and Fe II λ2814.45 could also be due to a larger optical depth in a chromospheric condensation: in this case, the redshifted component to the emergent intensity would be relatively brighter compared to the component of the intensity originating from the stationary flare layers below. There may also be a different brightness evolution in He I due to the variation in
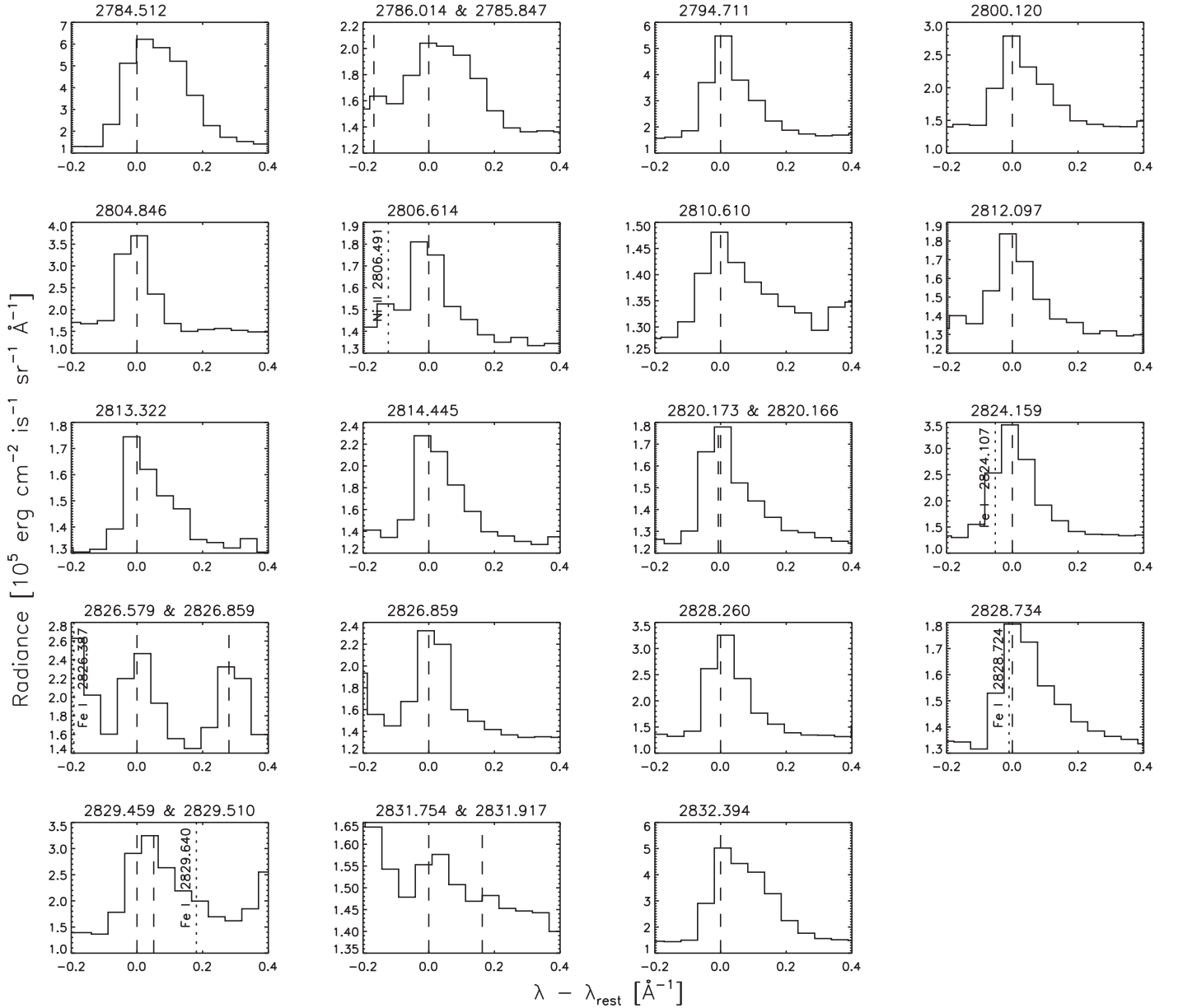
Figure 9. Line profiles in the NUV spectrum of UFB-3 for all definitively identified Fe II lines. All wavelength scales are from -0.2 to 0.4 Å from the rest wavelength, where the stronger Fe II line is used when two are present. Rest wavelengths of Fe II lines and other blends are indicated by dashed and dotted lines, respectively. Many of the Fe II profiles exhibit a red-wing asymmetry with more spectral bins with an intensity greater than or equal to the line half-maximum on the red side than on the blue side.

temperature sensitivity among different species formed in a condensation cooling from high to low temperature. Ostensibly, He I lines probe higher temperatures than Fe II, Mg II, and the NUV continuum radiation but detailed modeling is necessary to account for non-equilibrium ionization of helium (Allred et al. 2005, 2015; Golding et al. 2014; Simões et al. 2016). Modeling of this line will be included in Paper II.

5. Summary and Discussion

In this paper, we present a comprehensive analysis of umbral flare ribbon spectra in the NUV. These observations were obtained with a custom observing mode and high time resolution, thus allowing us to characterize the flare continuum enhancements and constrain the time evolution of heating in a single flaring location in the Sun. We present a new spectral ratio measurement, a continuum-to-line ratio, which can be obtained with NUV solar flare spectra with very limited wavelength coverage or large uncertainties in the intensity calibration. Because the Fe II $\lambda2814.45$ line and the NUV continuum radiation originate from (roughly) similar temperatures and exhibit (relatively) low optical depths in current RHD flare models (e.g., Kowalski et al. 2017a), the NUV continuum-to-line ratio (C2826′/Fe II $\lambda2814.45$) indicates the relative amounts of heating to $T \sim 10{,}000$ K at high column mass ($\log m/[\mathrm{g\,cm^{-2}}] \sim -2$) compared at moderate-to-low column mass ($\log m/[\mathrm{g\,cm^{-2}}] \sim -3$). This interpretation will be described in detail in Paper II with new RHD models. Further, the ratio is generally independent of the spatial resolution assuming that the Fe II $\lambda2814.45$ line and the C2826′ continuum radiation are produced at the same locations and
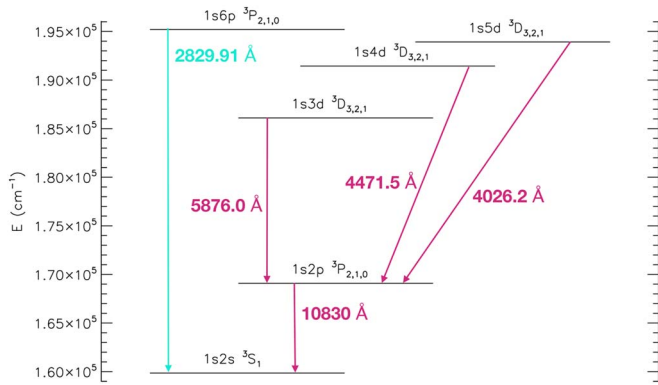
Figure 10. Partial term diagram showing several important flare lines in the triplet system of He I, including the $\lambda 2829.91$ multiplet in the *IRIS* SJI 2832 bandpass. For reference, the ionization energy of He I is 198,310.6664 cm^{-1} (Kandula et al. 2010).

do not exhibit different spatial structures below the instrumental resolution. Thus, the ratio facilitates a robust comparison of 1D models to observations that are spatially unresolved (as in dMe flares using the ratio of Hγ line flux to the blue 4170 Å continuum; Kowalski et al. 2013, 2019; Silverberg et al. 2016) or have low spatial resolution, in which case the value of the continuum intensity is not accurately inferred due to spatial smoothing.

In the umbral flare brightening spectra of the 2014 October 25 X1 flare, C2826′/Fe II $\lambda 2814.45 = 7-8$, which is a factor of seven to eight larger than in the hard X-ray impulsive phase spectra of the 2014 March 29 X1 flare: in the "BFP2" flare spectrum of the 2014 March 29 flare (Kowalski et al. 2017a), the C2826′/Fe II $\lambda 2814.45$ ratio is 1.0 but the value of C2826′ is nearly a factor of 20 larger than at the peak of UFB-3. A 5F11 RHD simulation was used to model the red-wing asymmetry and bright continuum radiation in the 2014 March 29 flare in Kowalski et al. (2017a). This model predicts a continuum-to-line ratio of 1.1 (with a microturbulence parameter) and 1.8 (without a microturbulence parameter) and thus does not explain the large values in the UFBs in the 2014 October 25 flare. In the 2014 March 29 flare, the Fe II $\lambda 2814.45$ line exhibits a very bright and broad red-wing component (see Figure 4(b)). A lack of a bright, spectrally resolved red wing component in the 2014 October 25 flare contributes to a larger C2826′/Fe II $\lambda 2814.45$, but this is not nearly enough to explain the large values. These shortcomings of the 5F11 RHD model motivate using the *Fermi*/GBM data to model the nonthermal electron parameters in the 2014 October 25 X1 flare. The *Fermi* X-ray data (Section 2.2) suggest a similar energy flux as for the 2014 March 29 flare (Kleint et al. 2016) but a much steeper power law index ($\delta = 8-9$ compared to 4).

The observed range of red-wing properties in X-class flares suggest that the SJI 2832 contributions from emission lines may be significantly different in other flares that produce a spectrally resolved, bright red-wing asymmetry in the Fe II, Cr II, and helium I lines, which all contribute to the SJI 2832 bandpass. In addition to providing detailed information on the contributions to the *IRIS* SJI 2832 during flares, we used the full readout data to characterize a He I flare line in the NUV. The helium emission will be used to provide constraints on the heating at higher temperatures than where Fe II and the NUV continuum form, and it will help understand the origin of the

nonthermal broadening in NUV flare lines. To our knowledge, this is the first report of this He I line in a solar flare.

6. Conclusions

We detect bona fide NUV continuum radiation in *IRIS* flare spectra with a contrast of 1000% in a solar umbra. The spectra were obtained during the fourth hard X-ray peak at $E > 35$ keV as a ribbon (which was part of a larger, three-ribbon X-class solar flare) developed into a sunspot. The main result of this analysis is the characterization of the ratio of NUV continuum radiation to the Fe II $\lambda 2814.45$ line-integrated intensity, obtained from the *IRIS* NUV spectra. This continuum-to-line ratio is a new diagnostic of the relative heating rates at high and low column mass in the flare chromosphere because they are formed over similar temperatures (Appendix A) with moderately different optical depths (see Kowalski et al. 2017a and Paper II). The ratios vary over values of $\approx 5-8$ in the umbral flare brightenings, attaining values of $\approx 7-8$ over the peak times. New RHD models are required to explain these large values, since previous high-beam flux models predict much lower values and highly redshifted Fe II emission line components (Kowalski et al. 2017a).

With the full spectral range of *IRIS*, we establish, for this flare, that the intensity in the narrow continuum window from $\lambda = 2824.5-2825.90$ Å (C2826) adequately represents the continuum level throughout the full NUV range of *IRIS*. We also identified the flare emission line landscape in the *IRIS* NUV and *IRIS* SJI 2832 images and found that the He I $\lambda 2829.9$ Å line becomes bright and broad in solar flares. This line is in the SJI 2832 wavelength range and requires full spectral readout of the *IRIS* NUV, as it is not included in standard *IRIS* linelists. Full spectral readout of the *IRIS* NUV also provides multiple lines of Fe II, Fe I, Cr II, and other species, yielding sets of profiles to constrain properties of the flaring solar atmosphere and disambiguate blends. The emission lines exhibit red profile asymmetries, but these are much less redshifted and broad than in another well-studied X-class flare with *IRIS* data.

The hard X-rays from *Fermi*/GBM, combined with an algorithm (from D. Graham et al. 2019, in preparation) to estimate the flare area, provide starting-point inputs into RHD flare models of these intriguing umbral flare brightenings, in order to determine if the *IRIS* NUV flare spectra can be explained by electron beam heating alone and whether significant photospheric heating is required to produce large continuum-to-line ratios. In Paper II, we will use these two constraints (the continuum-to-line ratio and the Fe II line profile asymmetries) in addition to the constraints at higher temperatures from He I $\lambda 2829.9$ to determine the relative heating in the photosphere, in the chromosphere at high column mass, and in the chromosphere at low column mass in solar flares.

Appendix A
The Formation of Fe II λ2814.45 and Continuum Radiation at λ = 2826 Å in LTE

In this appendix, we present the temperature and density sensitivities for hydrogen Balmer recombination radiation, the line intensity in Fe II λ2814.45, and their ratios. The similar temperature sensitivities (assuming LTE) justify using the Fe II λ2814.45 to constrain the velocity field in the layers where the NUV continuum radiation is formed, and the ratios from optically thin uniform slabs suggest that a more sophisticated approach to the modeling (e.g., with RHD models) is necessary.

We calculate the LTE, $\lambda = 2826$ Å hydrogen bound–free continuum emissivity and the Fe II λ2814.45 line-integrated emissivity for a range of gas densities (ρ) and temperatures (T). We use the standard equations from Rutten (2003), Aller (1963), and Mihalas (1978) (Equation (7–4)) for the spontaneous thermal, LTE line, and continuum emissivities. For hydrogen ($Z = 1$) recombination to a given principal quantum number n, the LTE continuum emissivity, j_λ, follows from $\alpha(\lambda)$ B_λ (where α is the opacity corrected for stimulated emission) and varies as $\lambda^{-2}e^{-\frac{hc}{\lambda kT}}g_{\mathrm{bf}}(\lambda)$ (see also Equation (3) of Kowalski et al. 2015b). Including the n dependence, the continuum emissivity reduces to the following:

$$j_{\lambda,\mathrm{b-f}} = \frac{6.48 \times 10^{-14}}{4\pi\lambda^2} \frac{n_e n_p}{T_e^{1.5} n^3} \exp\left[\frac{1.58 \times 10^5}{n^2 T_e} - \frac{1.44 \times 10^8}{\lambda T_e}\right] g_{\mathrm{bf}}(\lambda) \quad (1)$$

in units of erg s^{-1} cm^{-3} sr^{-1} Å^{-1}, and the units of wavelength are Angstroms. The values of the hydrogen bound–free gaunt factor ($g_{\mathrm{bf}}(\lambda)$) are taken from Seaton (1960). We calculate the recombination to $n = 2$; recombination to $n = 3$ and free–free emissivity contribute a moderate amount (20%) to the continuum emissivity only at the highest temperatures that we consider ($T = 22,000$ K). At the lowest temperatures, H$^-$ recombination may contribute at the highest densities (but is not included here).

For the spontaneous thermal line emissivity, we use Equations (2.69) of Rutten (2003) with n_{upper} calculated from LTE using the partition function of Halenka & Grabowski (1984) and the ionization potential lowered by 0.1 eV for Fe I and Fe II and 0.25 eV for Fe III. We integrate over the wavelength of the line (thus giving Equations (2.70) of Rutten 2003).

The emissivity grids are shown in Figure 11. For the same density, the bound–free emissivity peaks at slightly higher ($\Delta T \sim 1000$ K) temperature and has a relatively brighter tail at higher temperatures. However, the peaks in the continuum emissivity curves are rather broad: 90% of the maximum for each ρ value falls within the peak of the Fe II λ2814.45 emissivity, and at 50%, the emissivity of Fe II λ2814.45 spans the temperatures of 8000–18,000 K.
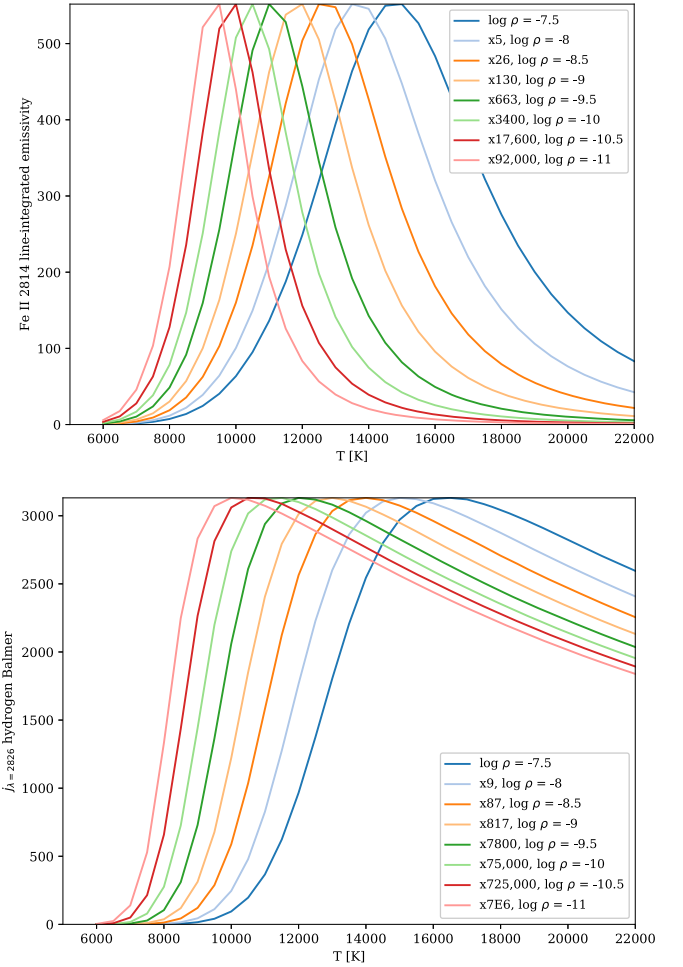
Figure 11. (Top) Thermal LTE Fe II λ2814.45 emissivity as a function of ρ [g cm^{-3}] and T [K]. (Bottom) Balmer continuum emissivity (recombination to $n = 2$) as a function of ρ and T, given by Equation (1). The free–free continuum emissivity and recombination to $n = 3$ are not included here; they each contribute only ~10% to the total emissivity at the highest temperatures over this temperature range. The legends indicate the scaling used to multiply each emissivity curve to the y-axis range for the log $\rho = -7.5$ curves.

In Figure 12, we show the ratios of the emissivities. This figure also gives the emergent intensity ratio from isothermal, isobaric optically thin, slab models in LTE. The ratios are typically much less than unity except at very high temperatures at $T > 16,000$ K. In RHD models (Kowalski et al. 2017a), the Fe II λ2814.45 line and NUV continuum radiation are formed at significantly lower temperatures than $T = 16,000$ K because most of the flare chromospheric mass is at lower temperatures. For example, about 95% of the emergent NUV continuum intensity originates from $T \leqslant 18,000$ K in the evolved chromospheric condensation in the 5F11 electron beam-heated model atmosphere in Kowalski et al. (2017a). Therefore, optically thin slab predictions over a reasonable temperature range do not explain the large continuum-to-line ratios in the UFBs. As we will show in Paper II, large optical depths from significant heating at high column mass can produce consistent continuum-to-line ratios.
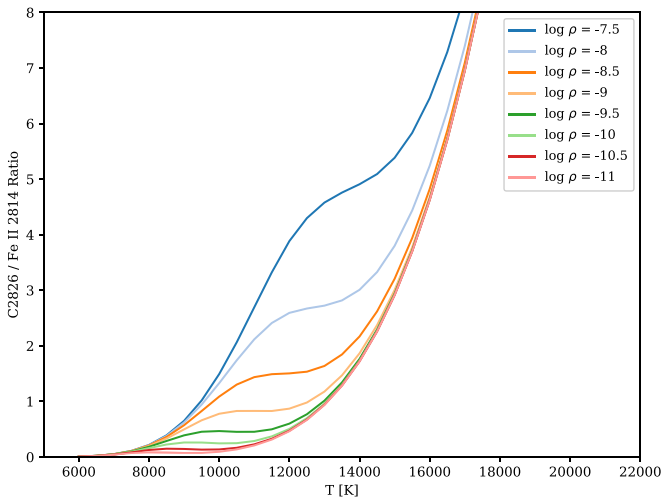
Figure 12. C2826/Fe II λ2814.45 emissivity (also, optically thin LTE emergent intensity) ratios as a function of ρ and T. In RHD model atmospheres, the ratios of the emergent intensity differ from these values due to non-uniform ρ and T as a function of height and time, possible non-equilibrium effects (e.g., non-LTE ionization of Fe II λ2814.45), and differences in the optical depth between the emergent C2826′ continuum radiation and the Fe II λ2814.45 emission line. These slab models do not reasonably explain the observed range of ratios (7–8; Figure 3) in the UFBs.

Appendix B
Flare Line Identifications in the *IRIS* NUV

A number of lines in the UFB-3 peak excess intensity spectrum are identified in Table 1 and shown in Figure 13. The line-integrated, continuum-subtracted line intensities were estimated by fitting the local continuum using a first-order polynomial and subtracting across the emission line(s). The 30% bisectors are calculated from the intensity after subtracting a local continuum (without subtracting a pre-flare spectrum) to indicate the measured wavelengths. In the last two rows, the excess continuum intensity, C2826′, and the *IRIS* NUV bandpass-integrated brightness are also given. Rest wavelengths for Fe II, Cr II, and Fe I are adopted primarily from Nave & Johansson (2013), Sansonetti & Nave (2014), and Nave et al. (1994), respectively, and additional data on wavelengths and *A*-values were obtained from the NIST (Kramida et al. 2018), Kurucz (2018), and R. L. Kelly (https://www.cfa.harvard.edu/ampcgi/kelly.pl) databases and references therein. Most observed species have more than one line in the *IRIS* NUV, and many have lines from the same multiplet. Consistency for each species was established by comparing line positions and profiles to those from the same species, and by comparing the observed intensity ratios for each species to those from Boltzmann-distributed populations for a range of temperatures of formation (e.g., 7000–22,000 K for Fe II; see Figure 11), that is, optically thin LTE calculations, with opacity considered in the comparisons as discussed below.

Of the 31 Fe II lines listed in the UFB-3 peak spectrum, the majority are reasonably strong, isolated features with no evidence of significant blends, providing many ratios between Fe II line intensities that can be used to constrain model atmospheres. As discussed in Section 4.3, compared to the ratios in the flare, the LTE intensity ratios are systematically over-predicted for the bright Fe II lines, and we speculate that optical depth in these brighter Fe II lines prevents a relatively larger amount of emission from escaping from the stationary flare layers below the chromospheric condensation. This speculation is supported by the fact that for the two brightest Fe II lines, λ2784.512 and λ2832.394, the rest component is less pronounced relative to the red wing than it is for the weaker Fe II lines (Figure 9). Recent electron impact excitation calculations by Tayal & Zatsarinny (2018) are now available for 25 of the 31 observed Fe II lines, and can be used to facilitate accurate modeling of these lines to test this hypothesis.

Two observed Fe II lines are not in fact listed in the most recent work by Nave & Johansson (2013): Fe II λ2820.173 and λ2828.724, although these most recent energy levels are certainly consistent with the observed wavelengths. In the case of Fe II 2820.173, the lack of an identification in the most recent laboratory work is possibly due to blending with the Fe II 2820.166 line, which is readily excited in laboratory spectra, but comes from a higher level of excitation than would be expected for solar plasmas. As with the other flare line identifications for UFB-3, evidence is provided by the similarity of the Fe II λ2820.173 and λ2828.724 profiles to other Fe II lines, and of intensity levels to preliminary LTE calculations. In this case, both these lines and Fe II λ2824.159 are from the same multiplet as well, so we are fairly confident of these identifications. There is an Fe I line at 2828.724 Å to be aware of, but it is expected to be an order of magnitude weaker than the other nearby observed lines of Fe I. The *A*-values reported by Kurucz (2018) and Fuhr & Wiese (2006) are in reasonable agreement for all of the *IRIS* NUV Fe II lines that are in both databases, although with differences in some cases of up to a factor of two. *A*-values for six of the lines, including λ2828.724, are reported only by Kurucz, so in Table 1 the *A*-values for those lines are from Kurucz, while the balance is from Fuhr & Wiese.

While the most extensive set of profiles is provided by Fe II, there are quite a few Cr II lines with profiles having red wings similar to those of Fe II, which provide another set of lines to test the hypothesis above by comparison to future modeling. Multiple lines of Fe I, Ti II, Ni I, Ni II, and Mn I are observed as well. Note that, like the He I 2829.91 Å line discussed in Section 4.4 and Mg II h and k, the Al II 2817.014 Å line peaks to the red in UFB-3. There is a line of Ti II in the red wing of Al II, but the intensities of the other observed lines of Ti II do not indicate that Ti II is a significant contribution to this Al II profile. Finally, note that O V is listed not as a definitive identification, but as a possible contribution to the feature around 2788 Å. If present, the O V 2787.814 Å line appears blended with other lines, and it would be accompanied by the weaker line from the same multiplet at 2790.669 Å, for which there is a blend with a weak Fe I line.

Interestingly, there is a line from a doubly excited state of He I that has been observed at 2819.2 ± 0.3 Å using beam-foil spectroscopy (Berry et al. 1972), which could conceivably contribute to the observed feature at that wavelength in the UFB-3 flare spectrum. In solar plasmas, such doubly excited states would be populated through electron capture by nonthermal (accelerated) helium ions upon hitting a thick

Table 1
Flare Line IDs in the *IRIS* NUV

Intensity $\left[\frac{10^3\ \text{erg}}{\text{cm}^2\ \text{s sr}}\right]$	Species[a]	λ_{rest} (Å)	Bis[b] (km s^{-1})	$J_l - J_u$	Multiplet	E_l (cm^{-1})	E_u (cm^{-1})	A-value (s^{-1})
112	Fe II	2784.512	7.5	11/2–9/2	$3d^6(^3\text{H})4s\ \text{b}^2\text{H}–3d^6(^3\text{H})4p\ z^2\text{G}^o$	26170.181	62083.118	1.06e+08
4	(Fe II)	2785.847	⋯	3/2–3/2	$3d^7\ \text{a}^4\text{F}–3d^6(^5\text{D})4p\ z^6\text{D}^o$	3117.488	39013.216	7.57e+03
19	Fe II	2786.014	4.4	11/2–9/2	$3d^6(^5\text{D})4p\ z^6\text{F}^o–3d^6(^5\text{D})5s\ \text{e}^6\text{D}$	41968.070	77861.650	1.53e+08
8	Cr II	2786.514	6.7	9/2–13//2	$3d^4(^3\text{G})4s\ \text{b}^4\text{G}–3d^4(^3\text{G})4p\ ^4\text{F}^o$	33618.936	69506.065	2.09e+08
24	(O V)	2787.814	8.3	1–1	$2s3s\ ^3\text{S}–2s3p\ ^3\text{P}^o$	546972.700	582843.100	1.41e+08
6	Cr II	2788.440	6.0	5/2–5/2	$3d^4(\text{a}^3\text{P})4s\ \text{b}^4\text{P}–3d^4(\text{a}^3\text{P})4p\ \text{y}^4\text{P}^o$	30864.433	66726.782	1.50e+08
19	Fe I	2788.927	0.7	5–6	$3d^7(^4\text{F})4s\ \text{a}^5\text{F}–3d^6(^3\text{H})4s4p(^3\text{P}^o)\ \text{y}^5\text{G}^o$	6928.268	42784.349	6.30e+07
2	(Fe I)	2790.624	⋯	5–4	$3d^7(^2\text{G})4s\ \text{a}^3\text{G}–3d^6(^3\text{D})4s4p(^3\text{P}^o)\ \text{t}^3\text{F}^o$	21715.731	57550.006	2.36e+07
⋯	(O V)	2790.669	⋯	1–0	$2s3s\ ^3\text{S}–2s3p\ ^3\text{P}^o$	546972.700	582806.400	1.43e+08
1175	Mg II	2791.600	8.2	1/2–3/2	$2p^63p\ ^2\text{P}^o–2p^63d\ ^2\text{D}$	35669.310	71491.063	4.08e+08
8	Cr II	2792.978	3.6	11/2–9/2	$3d^4(^3\text{G})4s\ \text{b}^4\text{G}–3d^4(^3\text{G})4p\ ^4\text{F}^o$	33694.142	69498.214	2.30e+08
53	Fe II	2794.711	3.2	9/2–11/2	$3d^6(^3\text{G})4s\ \text{a}^4\text{G}–3d^6(^3\text{H})4p\ z^4\text{I}^o$	25805.327	61587.205	1.30e+07
1	Mn I	2795.641	⋯	5/2–13//2	$3d^54s^2\ \text{a}^6\text{S}–3d^5(^6\text{S})4s4p(^1\text{P}^o)\ \text{y}^6\text{P}^o$	0.000	35769.970	3.62e+08
7036	Mg II	2796.352	9.9	1/2–3/2	$2p^63s\ ^2\text{S}–2p^63p\ ^2\text{P}^o$	0.000	35760.880	2.68e+08
2	(Fe II)	2797.868	⋯	3/2–5/2	$3d^7\ \text{a}^4\text{F}–3d^6(^5\text{D})4p\ z^6\text{D}^o$	3117.488	38858.970	2.02e+03
⋯	Mg II	2798.754	⋯	3/2–3/2	$2p^63p\ ^2\text{P}^o–2p^63d\ ^2\text{D}$	35760.880	71491.063	8.09e+07
1683	Mg II	2798.823	6.0	3/2–5/2	$2p^63p\ ^2\text{P}^o–2p^63d\ ^2\text{D}$	35760.880	71490.190	4.81e+08
1	Ni I	2799.474	⋯	2–2	$3d^9(^2\text{D})4s\ ^3\text{D}–3d^8(^3\text{F})4s4p(^3\text{P}^o)\ ^1\text{D}^o$	879.813	36600.805	5.77e+06
20	Fe II	2800.120	3.8	9/2–13//2	$3d^6(^3\text{H})4s\ \text{b}^2\text{H}–3d^6(^3\text{F2})4py^4\text{F}^o$	26352.767	62065.528	1.55e+07
3	(Fe II)	2800.548	5.4	9/2–9/2	$3d^6(^3\text{G})4s\ \text{a}^4\text{G}–3d^6(^3\text{H})4p\ z^4\text{I}^o$	25805.327	61512.630	5.00e+05
10	Cr II	2801.591	7.3	11/2–13/2	$3d^4(^3\text{G})4s\ \text{b}^4\text{G}–3d^4(^3\text{G})4p\ \text{y}^4\text{H}^o$	33694.142	69388.151	2.20e+08
7	Mn I	2801.907	−0.4	5/2–3/2	$3d^54s^2\ \text{a}^6\text{S}–3d^5(^6\text{S})4s4p(^1\text{P}^o)\ \text{y}^6\text{P}^o$	0.000	35689.980	3.69e+08
6169	Mg II	2803.531	10.8	1/2–1/2	$2p^63s\ ^2\text{S}–2p^63p\ ^2\text{P}^o$	0.000	35669.310	2.62e+08
23	Fe II	2804.846	−0.4	5/2–5/2	$3d^6(^3\text{F2})4s\ \text{a}^2\text{F}–3d^6(^3\text{F2})4p\ \text{x}^4\text{D}^o$	27620.403	63272.981	1.60e+06
7	Fe I	2805.347	−0.5	4–4	$3d^7(^4\text{F})4s\ \text{a}^5\text{F}–3d^6(^3\text{H})4s4p(^3\text{P}^o)\ \text{y}^5\text{G}^o$	7376.764	43022.982	1.05e+07
1	(Fe II)	2805.826	⋯	7/2–5/2	$3d^6(^3\text{F2})4p\ \text{y}^2\text{G}^o–3d^6(^3\text{F2})5s\ \text{e}^2\text{F}$	65109.691	100749.825	1.39e+08
1	(Fe II)	2806.145	⋯	3/2–5/2	$3d^6(^3\text{D})4s\ \text{b}^4\text{D}–3d^6(^3\text{F2})4p\ \text{y}^2\text{D}^o$	31364.455	67000.530	2.50e+06
1	Ni II	2806.491	⋯	9/2–13//2	$3d^8(^1\text{G})4s\ ^2\text{G}–3d^8(^1\text{D})4p\ ^2\text{F}^o$	32499.530	68131.210	1.30e+07
5	Fe II	2806.614	−0.9	7/2–13//2	$3d^6(^3\text{F2})4s\ \text{a}^2\text{F}–3d^6(^3\text{F2})4p\ \text{x}^4\text{D}^o$	27314.918	62945.045	3.20e+06
9	Fe I	2807.811	0.0	4–5	$3d^7(^4\text{F})4s\ \text{a}^5\text{F}–3d^6(^3\text{H})4s4p(^3\text{P}^o)\ z^5\text{H}^o$	7376.764	42991.694	1.15e+07
4	Fe II	2810.610	5.9	7/2–13//2	$3d^6(^5\text{D})4p\ z^6\text{P}^o–3d^6(^5\text{D})5s\ \text{e}^6\text{D}$	42658.244	78237.709	3.10e+07
3	Ti II	2811.061	2.6	7/2–9/2	$3d^2(^3\text{F})4p\ z^4\text{G}^o–3d^2(^3\text{F})4d\ \text{e}^4\text{H}$	29734.540	65308.300	5.09e+08
1	Ti II	2811.133	⋯	3/2–3/2	$3d^3\ \text{a}^2\text{P}–3d^2(^3\text{P})4p\ \text{y}^2\text{P}^o$	9975.920	45548.760	1.24e+07
8	Fe II	2812.097	0.8	11/2–9/2	$3d^6(^3\text{G})4s\ \text{a}^4\text{G}–3d^6(^3\text{H})4p\ z^4\text{H}^o$	25428.789	60989.444	1.20e+06
9	Cr II	2812.828	7.9	9/2–11/2	$3d^4(^3\text{G})4s\ \text{b}^4\text{G}–3d^4(^3\text{G})4p\ \text{y}^4\text{H}^o$	33618.936	69170.353	2.05e+08
6	Fe II	2813.322	4.8	3/2–3/2	$3d^6(^3\text{P2})4s\ \text{b}^2\text{P}–3d^6(^3\text{P2})4p\ \text{y}^4\text{P}^o$	25787.582	61332.753	2.90e+06
11	Fe I	2814.115	0.1	4–5	$3d^7(^4\text{F})4s\ \text{a}^5\text{F}–3d^6(^3\text{H})4s4p(^3\text{P}^o)\ \text{y}^5\text{G}^o$	7376.764	42911.914	3.42e+07
15	Fe II	2814.445	3.7	7/2–9/2	$3d^6(^3\text{G})4s\ \text{a}^4\text{G}–3d^6(^3\text{H})4p\ z^4\text{I}^o$	25981.645	61512.630	3.40e+06
22	Al II	2817.014	10.9	1–0	$3s3p\ ^1\text{P}^o–3s4s\ ^1\text{S}$	59852.020	95350.600	3.93e+08
1	Cr II	2817.670	⋯	5/2–3/2	$3d^4(\text{a}^3\text{P})4s\ \text{b}^4\text{P}–3d^4(\text{a}^3\text{P})4p\ \text{y}^4\text{P}^o$	30864.433	66354.757	1.04e+08
1	(Fe II)	2817.916	⋯	5/2–3/2	$3d^6(^5\text{D})4p\ z^6\text{P}^o–3d^6(^5\text{D})5s\ \text{e}^6\text{D}$	43238.607	78725.822	3.40e+07
7	Cr II	2819.184	7.4	7/2–9/2	$3d^4(^3\text{G})4s\text{b}^4\text{G}–3d^4(^3\text{G})4p\ \text{y}^4\text{H}^o$	33521.090	68992.347	2.21e+08
⋯	Fe II	2820.166	⋯	5/2–5/2	$3d^6(^3\text{D})4p\ \text{x}^2\text{D}^o–3d^6(^3\text{G})4d\ ^2\text{D}$	74606.864	110065.766	8.25e+05
8	Fe II	2820.173	2.7	11/2–11/2	$3d^6(^3\text{G})4s\ \text{a}^4\text{G}–3d^6(^3\text{H})4p\ z^4\text{H}^o$	25428.784	60887.598	1.00e+06
2	Ni I	2822.120	0.6	3–3	$3d^9(^2\text{D})4s\ ^3\text{D}–3d^8(^3\text{F})4s4p(^3\text{P}^o)\ ^1\text{F}^o$	204.786	35639.148	4.87e+06
6	Cr II	2822.842	7.2	5/2–13//2	$3d^4(^3\text{G})4s\ \text{b}^4\text{G}–3d^4(^3\text{G})4p\ \text{y}^4\text{H}^o$	33417.981	68843.273	2.29e+08
28	Cr II	2823.199	7.6	13/2–15/2	$3d^4(^3\text{H})4s\ \text{a}^4\text{H}–3d^4(^3\text{H})4p\ z^4\text{I}^o$	30391.831	65812.649	2.28e+08
⋯	Fe I	2824.107	⋯	3–3	$3d^7(^4\text{F})4s\ \text{a}^5\text{F}–3d^6(^3\text{H})4s4p(^3\text{P}^o)\ \text{y}^5\text{G}^o$	7728.059	43137.484	1.51e+07
30	Fe II	2824.159	0.2	11/2–13/2	$3d^6(^3\text{G})4s\ \text{a}^4\text{G}–3d^6(^3\text{H})4p\ z^4\text{H}^o$	25428.789	60837.560	2.10e+06
3	Ni II	2826.062	−0.3	5/2–5/2	$3d^8(^3\text{P})4s\ ^4\text{P}–3d^8(^3\text{F})4p\ ^2\text{F}^o$	23108.280	58493.210	2.65e+06
14	Fe I	2826.387	1.3	3–4	$3d^7(^4\text{F})4s\ \text{a}^5\text{F}–3d^6(^3\text{H})4s4p(^3\text{P}^o)\ z^5\text{H}^o$	7728.059	43108.914	1.32e+07
18	Fe II	2826.579	0.5	11/2–9/2	$3d^6(^3\text{G})4s\ \text{a}^4\text{G}–3d^6(^3\text{H})4p\ z^4\text{G}^o$	25428.789	60807.239	1.40e+06
16	Fe II	2826.859	1.6	7/2–5/2	$3d^6(^3\text{F2})4s\ \text{a}^2\text{F}–3d^6(^3\text{P2})4p\ \text{y}^4\text{D}^o$	27314.918	62689.874	4.50e+06
25	Fe II	2828.260	2.3	11/2–13/2	$3d^6(^3\text{H})4s\ \text{b}^2\text{H}–3d^6(^3\text{H})4p\ z^4\text{I}^o$	26170.181	61527.610	2.40e+06
⋯	Fe I	2828.724	⋯	3–4	$3d^64s^2\ \text{a}^5\text{D}–3d^7(^4\text{F})4p\ z^3\text{G}^o$	415.933	35767.562	1.48e+05
7	Fe II	2828.734	5.2	9/2–13//2	$3d^6(^3\text{G})4s\ \text{a}^4\text{G}–3d^6(^3\text{H})4p\ z^4\text{H}^o$	25805.328	61156.835	1.51e+06
36	Fe II	2829.459	⋯	11/2–9/2	$3d^6(^3\text{H})4s\ \text{b}^2\text{H}–3d^6(^3\text{H})4p\ z^4\text{I}^o$	26170.181	61512.630	6.90e+06

15

Table 1
(Continued)

Intensity $\left[\frac{10^3 \text{ erg}}{\text{cm}^2 \text{ s sr}}\right]$	Species[a]	λ_{rest} (Å)	Bis[b] (km s^{-1})	$J_l - J_u$	Multiplet	E_l (cm^{-1})	E_u (cm^{-1})	A-value (s^{-1})
⋯	Fe II	2829.510	2.5	5/2–3/2	$3d^6(^3F2)4s$ a^{2}F–$3d^6(^3P2)4p$ y^{4}D^o	27620.403	62962.215	9.00e+06
⋯	Fe I	2829.640	⋯	2–3	$3d^7(^4F)4s$ a^{5}F–$3d^6(^3H)4s4p(^3P^o)$ z^{5}H^o	7985.784	43325.961	1.87e+06
⋯	He I	2829.911	⋯	1–0	$1s2s$ ^{3}S–$1s6p$ ^{3}P^o	159855.974	195192.777	1.94e+06
81	He I	2829.913	10.9	1–1	$1s2s$ ^{3}S–$1s6p$ ^{3}P^o	159855.974	195192.746	1.94e+06
⋯	He I	2829.914	⋯	1–2	$1s2s$ ^{3}S–$1s6p$ ^{3}P^o	159855.974	195192.743	1.94e+06
27	Cr II	2831.299	9.3	11/2–13/2	$3d^4(^3H)4s$ a^{4}H–$3d^4(^3H)4p$ z^{4}I^o	30298.468	65617.946	2.54e+08
⋯	Cr II	2831.449	⋯	13/2–11/2	$3d^4(^3H)4s$ a^{4}H–$3d^4(a^3F)4p$ z^{4}G^o	30391.831	65709.442	3.71e+07
3	Fe II	2831.754	⋯	7/2–5/2	$3d^6(^3G)4s$ b^{2}G–$3d^6(^3G)4p$ x^{4}G^o	30764.474	66078.272	7.00e+05
⋯	Fe II	2831.917	⋯	1/2–3/2	$3d^6(^3P2)4s$ b^{2}P–$3d^6(^3F2)4p$ y^{4}F^o	26932.735	62244.515	5.43e+05
71	Fe II	2832.394	7.3	3/2–5/2	$3d^6(^3P2)4s$ b^{2}P–$3d^6(^3P2)4p$ z^{2}D^o	25787.582	61093.406	7.60e+07
6	Ti II	2833.015	2.6	5/2–5/2	$3d^2(^3F)4s$ a^{2}F–$3d^2(^1D)4p$ y^{2}F^o	4628.580	39926.660	2.46e+07
11	Fe I	2833.269	3.7	3–4	$3d^7(^4F)4s$ a^{5}F–$3d^6(^3H)4s4p(^3P^o)$ y^{5}G^o	7728.059	43022.982	2.38e+07
⋯	Cr II	2833.287	⋯	11/2–9/2	$3d^4(^3H)4s$ a^{2}H–$3d^4(a^3F)4p$ y^{2}G^o	34812.926	70107.623	1.29e+08
1	(Fe II)	2833.918	⋯	5/2–5/2	$3d^6(^5D)4p$ z^{6}P^o–$3d^6(^5D)5s$ e^{6}D	43238.607	78525.442	4.50e+07
7	(Fe II)	2834.203	⋯	7/2–5/2	$3d^6(^5D)4s$ a^{4}D–$3d^6(^5D)4p$ z^{6}P^o	7955.319	43238.607	4.41e+04
1	(Fe II)	2834.681	⋯	5/2–3/2	$3d^6(^3G)4s$ a^{4}G–$3d^6(^3P2)4p$ y^{4}P^o	26055.412	61332.753	1.33e+05
124[c]	C2826′	2824.5–2825.9	⋯	⋯	⋯			
6200	NUV cont	2785–2835	⋯	⋯	⋯			

Notes.

[a] Parentheses indicate identifications that are not definitive. No intensity value is given for lines that are highly blended and are not a primary contribution to the observed feature.

[b] Measured wavelengths for this spectrum are given in the Bis column, which is the 30% bisector of a line. Bisector values are not given for lines that are likely not a main contribution to the observed feature, and they are not given for very low line intensities. For some fainter lines, a value of 1 can be estimated for the intensity. For Fe II 2786.014, 2806.614, and 2826.579, we use a Gaussian centroid for the measured wavelength because the 30% bisector extends across other blended lines. We adopt a representative centroiding uncertainty of 2.3–3.2 km s^{-1} as our statistical uncertainty, and the systematic uncertainty from the centroid of the Ni I absorption line in the quiet Sun (see Section 2.1) is 1.8 km s^{-1}.

[c] The value of C2826′ is given in units of 10^3erg cm^{-2} s^{-1} sr^{-1} Å^{-1}.

target, but not in thermal plasmas. Unfortunately, while there are stronger such lines outside the *IRIS* NUV bandpass, this one has a blend with Cr II 2819.18, which is the dominant contribution to the observed feature. It is nevertheless possible upon further evaluation of all the Cr II profiles that some evidence of a contribution from doubly excited helium in that

profile would provide a signature of accelerated helium ion beams.

In summary, a number of *IRIS* NUV lines are identified in this appendix that will be useful to model and compare to the data in order to constrain the physical structure of the flaring atmosphere observed by the *IRIS* spectrograph.
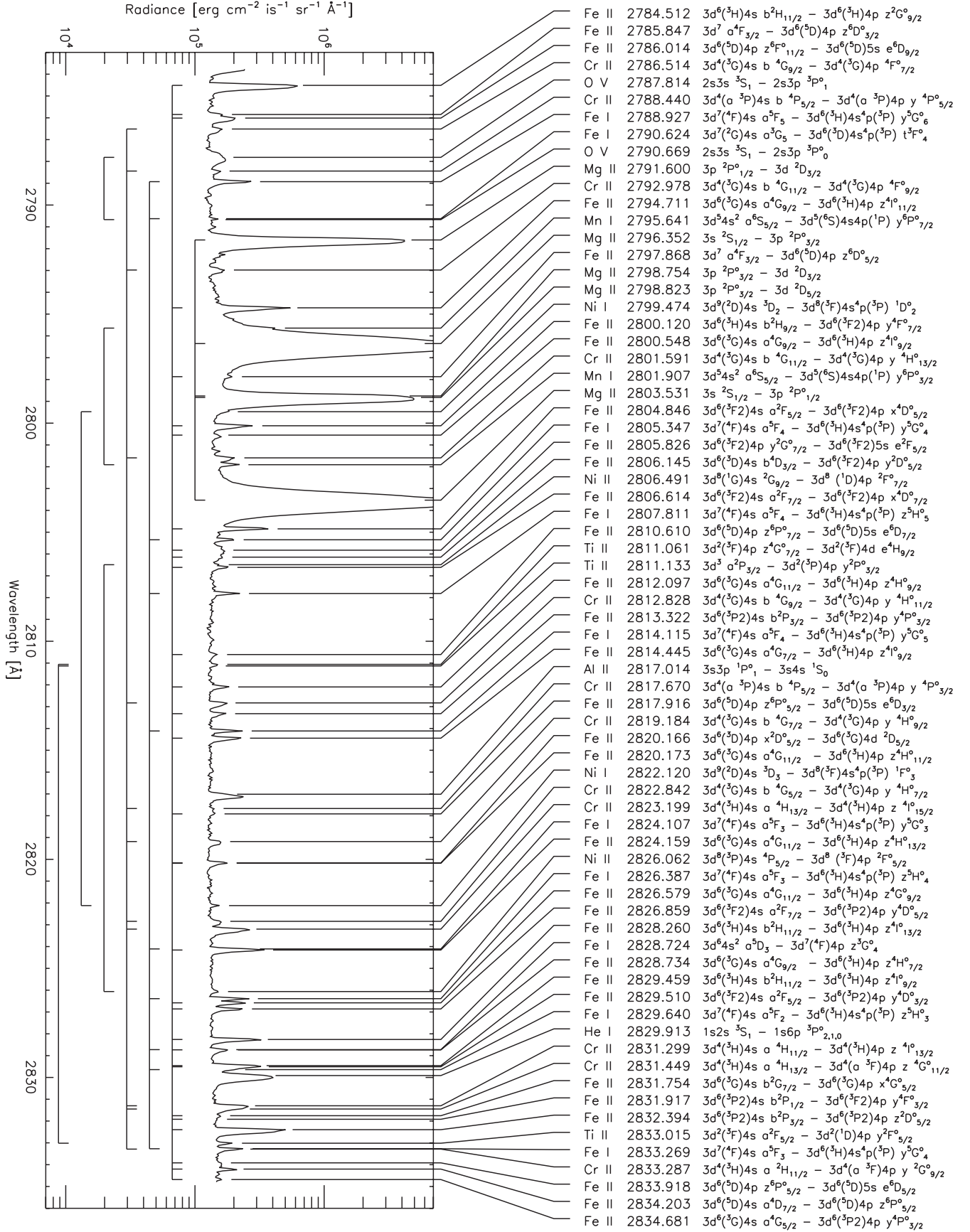
Radiance [erg cm^{-2} is^{-1} sr^{-1} Å^{-1}]

Wavelength [Å]

Fe II	2784.512	3d^6(^{3}H)4s b^{2}H$_{11/2}$ − 3d^6(^{3}H)4p z^{2}G$^o_{9/2}$
Fe II	2785.847	3d^7 a^{4}F$_{3/2}$ − 3d^6(^{5}D)4p z^{6}D$^o_{3/2}$
Fe II	2786.014	3d^6(^{5}D)4p z^{6}F$^o_{11/2}$ − 3d^6(^{5}D)5s e^{6}D$_{9/2}$
Cr II	2786.514	3d^4(^{3}G)4s b ^{4}G$_{9/2}$ − 3d^4(^{3}G)4p ^{4}F$^o_{7/2}$
O V	2787.814	2s3s ^{3}S$_1$ − 2s3p ^{3}P$^o_1$
Cr II	2788.440	3d^4(a ^{3}P)4s b ^{4}P$_{5/2}$ − 3d^4(a ^{3}P)4p y ^{4}P$^o_{5/2}$
Fe I	2788.927	3d^7(^{4}F)4s a^{5}F$_5$ − 3d^6(^{3}H)4s4p(^{3}P) y^{5}G$^o_6$
Fe I	2790.624	3d^7(^{2}G)4s a^{3}G$_5$ − 3d^6(^{5}D)4s4p(^{3}P) t^{3}F$^o_4$
O V	2790.669	2s3s ^{3}S$_1$ − 2s3p ^{3}P$^o_0$
Mg II	2791.600	3p ^{2}P$^o_{1/2}$ − 3d ^{2}D$_{3/2}$
Cr II	2792.978	3d^4(^{3}G)4s b ^{4}G$_{11/2}$ − 3d^4(^{3}G)4p ^{4}F$^o_{9/2}$
Fe II	2794.711	3d^6(^{3}G)4s a^{4}G$_{9/2}$ − 3d^6(^{3}H)4p z^{4}I$^o_{11/2}$
Mn II	2795.641	3d^{5}4s^2 a^{6}S$_{5/2}$ − 3d^5(^{6}S)4s4p(^{1}P) y^{6}P$^o_{7/2}$
Mg II	2796.352	3s ^{2}S$_{1/2}$ − 3p ^{2}P$^o_{3/2}$
Fe II	2797.868	3d^7 a^{4}F$_{3/2}$ − 3d^6(^{5}D)4p z^{6}D$^o_{5/2}$
Mg II	2798.754	3p ^{2}P$^o_{3/2}$ − 3d ^{2}D$_{3/2}$
Mg II	2798.823	3p ^{2}P$^o_{3/2}$ − 3d ^{2}D$_{5/2}$
Ni I	2799.474	3d^9(^{2}D)4s ^{3}D$_2$ − 3d^8(^{3}F)4s4p(^{3}P) ^{1}D$^o_2$
Fe II	2800.120	3d^6(^{3}H)4s b^{2}H$_{9/2}$ − 3d^6(^{3}F2)4p y^{4}F$^o_{7/2}$
Fe II	2800.548	3d^6(^{3}G)4s a^{4}G$_{9/2}$ − 3d^6(^{3}H)4p z^{4}I$^o_{9/2}$
Cr II	2801.591	3d^4(^{3}G)4s b ^{4}G$_{11/2}$ − 3d^4(^{3}G)4p y ^{4}H$^o_{13/2}$
Mn I	2801.907	3d^{5}4s^2 a^{6}S$_{5/2}$ − 3d^5(^{6}S)4s4p(^{1}P) y^{6}P$^o_{3/2}$
Mg II	2803.531	3s ^{2}S$_{1/2}$ − 3p ^{2}P$^o_{1/2}$
Fe II	2804.846	3d^6(^{3}F2)4s a^{2}F$_{5/2}$ − 3d^6(^{3}F2)4p x^{4}D$^o_{5/2}$
Fe I	2805.347	3d^7(^{4}F)4s a^{5}F$_4$ − 3d^6(^{3}H)4s4p(^{3}P) y^{5}G$^o_4$
Fe II	2805.826	3d^6(^{3}F2)4p y^{2}G$^o_{7/2}$ − 3d^6(^{3}F2)5s e^{2}F$_{5/2}$
Fe II	2806.145	3d^6(^{5}D)4s b^{4}D$_{3/2}$ − 3d^6(^{3}F2)4p y^{2}D$^o_{5/2}$
Ni II	2806.491	3d^8(^{1}G)4s ^{2}G$_{9/2}$ − 3d^8 (^{1}D)4p ^{2}F$^o_{7/2}$
Fe II	2806.614	3d^6(^{3}F2)4s a^{2}F$_{7/2}$ − 3d^6(^{3}F2)4p x^{4}D$^o_{7/2}$
Fe I	2807.811	3d^7(^{4}F)4s a^{5}F$_4$ − 3d^6(^{3}H)4s4p(^{3}P) z^{5}H$^o_5$
Fe II	2810.610	3d^6(^{5}D)4p z^{6}P$^o_{7/2}$ − 3d^6(^{5}D)5s e^{6}D$_{7/2}$
Ti II	2811.061	3d^2(^{3}F)4p z^{4}G$^o_{7/2}$ − 3d^2(^{3}F)4d e^{4}H$_{9/2}$
Ti II	2811.133	3d^3 a^{2}P$_{3/2}$ − 3d^2(^{3}P)4p y^{2}P$^o_{3/2}$
Fe II	2812.097	3d^6(^{3}G)4s a^{4}G$_{11/2}$ − 3d^6(^{3}H)4p z^{4}H$^o_{9/2}$
Cr II	2812.828	3d^4(^{3}G)4s b ^{4}G$_{9/2}$ − 3d^4(^{3}G)4p y ^{4}H$^o_{11/2}$
Fe II	2813.322	3d^6(^{3}P2)4s b^{2}P$_{3/2}$ − 3d^6(^{3}P2)4p y^{4}P$^o_{3/2}$
Fe I	2814.115	3d^7(^{4}F)4s a^{5}F$_4$ − 3d^6(^{3}H)4s4p(^{3}P) y^{5}G$^o_5$
Fe II	2814.445	3d^6(^{3}G)4s a^{4}G$_{7/2}$ − 3d^6(^{3}H)4p z^{4}I$^o_{9/2}$
Al II	2817.014	3s3p ^{1}P$^o_1$ − 3s4s ^{1}S$_0$
Cr II	2817.670	3d^4(a ^{3}P)4s b ^{4}P$_{5/2}$ − 3d^4(a ^{3}P)4p y ^{4}P$^o_{3/2}$
Fe II	2817.916	3d^6(^{5}D)4p z^{6}P$^o_{5/2}$ − 3d^6(^{5}D)5s e^{6}D$_{3/2}$
Cr II	2819.184	3d^4(^{3}G)4s b ^{4}G$_{7/2}$ − 3d^4(^{3}G)4p y ^{4}H$^o_{9/2}$
Fe II	2820.166	3d^6(^{3}G)4p x^{2}D$^o_{5/2}$ − 3d^6(^{3}G)4d ^{2}D$_{5/2}$
Fe II	2820.173	3d^6(^{3}G)4s a^{4}G$_{11/2}$ − 3d^6(^{3}H)4p z^{4}H$^o_{11/2}$
Ni I	2822.120	3d^9(^{2}D)4s ^{3}D$_3$ − 3d^8(^{3}F)4s4p(^{3}P) ^{1}F$^o_3$
Cr II	2822.842	3d^4(^{3}G)4s b ^{4}G$_{5/2}$ − 3d^4(^{3}G)4p y ^{4}H$^o_{7/2}$
Cr II	2823.199	3d^4(^{3}H)4s a ^{4}H$_{13/2}$ − 3d^4(^{3}H)4p z ^{4}I$^o_{15/2}$
Fe I	2824.107	3d^7(^{4}F)4s a^{5}F$_3$ − 3d^6(^{3}H)4s4p(^{3}P) y^{5}G$^o_3$
Fe II	2824.159	3d^6(^{3}G)4s a^{4}G$_{11/2}$ − 3d^6(^{3}H)4p z^{4}H$^o_{13/2}$
Ni I	2826.062	3d^8(^{3}P)4s ^{4}P$_{5/2}$ − 3d^8 (^{3}F)4p ^{2}F$^o_{5/2}$
Fe I	2826.387	3d^7(^{4}F)4s a^{5}F$_3$ − 3d^6(^{3}H)4s4p(^{3}P) z^{5}H$^o_4$
Fe II	2826.579	3d^6(^{3}G)4s a^{4}G$_{11/2}$ − 3d^6(^{3}H)4p z^{4}G$^o_{9/2}$
Fe II	2826.859	3d^6(^{3}F2)4s a^{2}F$_{7/2}$ − 3d^6(^{3}P2)4p y^{4}D$^o_{5/2}$
Fe II	2828.260	3d^6(^{3}H)4s b^{2}H$_{11/2}$ − 3d^6(^{3}H)4p z^{4}I$^o_{13/2}$
Fe I	2828.724	3d^{6}4s^2 a^{5}D$_3$ − 3d^7(^{4}F)4p z^{3}G$^o_4$
Fe II	2828.734	3d^6(^{3}G)4s a^{4}G$_{9/2}$ − 3d^6(^{3}H)4p z^{4}H$^o_{7/2}$
Fe II	2829.459	3d^6(^{3}H)4s b^{2}H$_{11/2}$ − 3d^6(^{3}H)4p z^{4}I$^o_{9/2}$
Fe II	2829.510	3d^6(^{3}F2)4s a^{2}F$_{5/2}$ − 3d^6(^{3}P2)4p y^{4}D$^o_{3/2}$
Fe I	2829.640	3d^7(^{4}F)4s a^{5}F$_2$ − 3d^6(^{3}H)4s4p(^{3}P) z^{5}H$^o_3$
He I	2829.913	1s2s ^{3}S$_1$ − 1s6p ^{3}P$^o_{2,1,0}$
Cr II	2831.299	3d^4(^{3}H)4s a ^{4}H$_{11/2}$ − 3d^4(^{3}H)4p z ^{4}I$^o_{13/2}$
Cr II	2831.449	3d^4(^{3}H)4s a ^{4}H$_{13/2}$ − 3d^4(a ^{3}F)4p z ^{4}G$^o_{11/2}$
Fe II	2831.754	3d^6(^{3}G)4s b^{2}G$_{7/2}$ − 3d^6(^{3}G)4p x^{4}G$^o_{5/2}$
Fe II	2831.917	3d^6(^{3}P2)4s b^{2}P$_{1/2}$ − 3d^6(^{3}F2)4p y^{4}F$^o_{3/2}$
Fe II	2832.394	3d^6(^{3}P2)4s b^{2}P$_{3/2}$ − 3d^6(^{3}P2)4p z^{2}D$^o_{5/2}$
Ti II	2833.015	3d^2(^{3}F)4s a^{2}F$_{5/2}$ − 3d^2(^{1}D)4p y^{2}F$^o_{5/2}$
Fe I	2833.269	3d^7(^{4}F)4s a^{5}F$_3$ − 3d^6(^{3}H)4s4p(^{3}P) y^{5}G$^o_4$
Cr II	2833.287	3d^4(^{3}H)4s a ^{2}H$_{11/2}$ − 3d^4(a ^{3}F)4p y ^{2}G$^o_{9/2}$
Fe II	2833.918	3d^6(^{5}D)4p z^{6}P$^o_{5/2}$ − 3d^6(^{5}D)5s e^{6}D$_{5/2}$
Fe II	2834.203	3d^6(^{5}D)4s a^{4}D$_{7/2}$ − 3d^6(^{5}D)4p z^{6}P$^o_{5/2}$
Fe II	2834.681	3d^6(^{3}G)4s a^{4}G$_{5/2}$ − 3d^6(^{3}P2)4p y^{4}P$^o_{3/2}$

Figure 13. *IRIS* NUV excess spectrum at the peak of UFB-3, showing all the lines identified in Table 1. The brackets on the left indicate multiple observable lines from the same species.

ORCID iDs

Adam F. Kowalski ⓘ https://orcid.org/0000-0001-7458-1176
Adrian N. Daw ⓘ https://orcid.org/0000-0002-9288-6210
Joel C. Allred ⓘ https://orcid.org/0000-0003-4227-6809
Graham S. Kerr ⓘ https://orcid.org/0000-0001-5316-914X
Gianna Cauzzi ⓘ https://orcid.org/0000-0002-6116-7301

References

Acampa, E., Smaldone, L. A., Sambuco, A. M., & Falciani, R. 1982, A&AS, 47, 485
Aller, L. H. 1963, Astrophysics. The atmospheres of the Sun and stars (New York: Ronald Press)
Allred, J. C., Hawley, S. L., Abbett, W. P., & Carlsson, M. 2005, ApJ, 630, 573
Allred, J. C., Hawley, S. L., Abbett, W. P., & Carlsson, M. 2006, ApJ, 644, 484
Allred, J. C., Kowalski, A. F., & Carlsson, M. 2015, ApJ, 809, 104
Amari, T., Canou, A., Aly, J.-J., Delyon, F., & Alauzet, F. 2018, Natur, 554, 211
Aschwanden, M. J. 1996, in AIP Conf Ser. 374, High energy solar physics, ed. R. Ramaty, N. Mandzhavidze, & X.-M. Hua (Melville, NY: AIP), 300
Aschwanden, M. J., Hudson, H., Kosugi, T., & Schwartz, R. A. 1996a, ApJ, 464, 985
Aschwanden, M. J., Kliem, B., Schwarz, U., et al. 1998a, ApJ, 505, 941
Aschwanden, M. J., Kosugi, T., Hudson, H. S., Wills, M. J., & Schwartz, R. A. 1996b, ApJ, 470, 1198
Aschwanden, M. J., & Schwartz, R. A. 1995, ApJ, 455, 699
Aschwanden, M. J., Schwartz, R. A., & Alt, D. M. 1995, ApJ, 447, 923
Aschwanden, M. J., Schwartz, R. A., & Dennis, B. R. 1998b, ApJ, 502, 468
Aschwanden, M. J., Wills, M. J., Hudson, H. S., Kosugi, T., & Schwartz, R. A. 1996c, ApJ, 468, 398
Bamba, Y., Inoue, S., Kusano, K., & Shiota, D. 2017, ApJ, 838, 134
Battaglia, M., & Kontar, E. P. 2011, A&A, 533, L2
Berry, H. G., Desesquelles, J., & Dufay, M. 1972, PhRvA, 6, 600
Boyer, R., Sotirovsky, P., Machado, M. E., & Rust, D. M. 1985, SoPh, 98, 255
Cheng, J. X., Ding, M. D., & Carlsson, M. 2010, ApJ, 711, 185
Courrier, H., Kankelborg, C., De Pontieu, B., & Wülser, J.-P. 2018, SoPh, 293, 125
Cram, L. E., & Woods, D. T. 1982, ApJ, 257, 269
De Pontieu, B., Title, A. M., Lemen, J. R., et al. 2014, SoPh, 289, 2733
Donati-Falchi, A., Falciani, R., & Smaldone, L. A. 1985, A&A, 152, 165
Donati-Falchi, A., Smaldone, L. A., & Falciani, R. 1984, A&A, 131, 256
Drake, G. 2006, in High Precision Calculations for Helium, ed. G. Drake (New York: Springer), 199
Dufton, P. L., & McKeith, C. D. 1980, A&A, 81, 8
Fahey, R. P. 1984, ApJS, 55, 507
Fisher, G. H. 1989, ApJ, 346, 1019
Fletcher, L., Hannah, I. G., Hudson, H. S., & Metcalf, T. R. 2007, ApJ, 656, 1187
Fuhr, J. R., & Wiese, W. L. 2006, JPCRD, 35, 1669
Gan, W. Q., Rieger, E., Zhang, H. Q., & Fang, C. 1992, ApJ, 397, 694
Golding, T. P., Carlsson, M., & Leenaarts, J. 2014, ApJ, 784, 30
Halenka, J., & Grabowski, B. 1984, A&AS, 57, 43
Hawley, S. L., & Fisher, G. H. 1992, ApJS, 78, 565
Hawley, S. L., & Pettersen, B. R. 1991, ApJ, 378, 725
Heinzel, P., & Kleint, L. 2014, ApJL, 794, L23
Heinzel, P., Kleint, L., Kašparová, J., & Krucker, S. 2017, ApJ, 847, 48
Hiei, E. 1982, SoPh, 80, 113
Hudson, H. S., Acton, L. W., Hirayama, T., & Uchida, Y. 1992, PASJ, 44, L77
Hudson, H. S., Wolfson, C. J., & Metcalf, T. R. 2006, SoPh, 234, 79
Hurford, G. J., Krucker, S., Lin, R. P., et al. 2006, ApJL, 644, L93
Inoue, S., Hayashi, K., & Kusano, K. 2016, ApJ, 818, 168
Kandula, D. Z., Gohle, C., Pinkert, T. J., Ubachs, W., & Eikema, K. S. E. 2010, PhRvL, 105, 063001
Kane, S. R., Love, J. J., Neidig, D. F., & Cliver, E. W. 1985, ApJL, 290, L45
Kerr, G. S., Fletcher, L., Russell, A. J. B., & Allred, J. C. 2016, ApJ, 827, 101
Kerr, G. S., Simões, P. J. A., Qiu, J., & Fletcher, L. 2015, A&A, 582, A50
Kleint, L., Heinzel, P., Judge, P., & Krucker, S. 2016, ApJ, 816, 88
Kleint, L., Heinzel, P., & Krucker, S. 2017, ApJ, 837, 160
Kontar, E. P., MacKinnon, A. L., Schwartz, R. A., & Brown, J. C. 2006, A&A, 446, 1157
Kowalski, A. F., & Allred, J. C. 2018, ApJ, 852, 61
Kowalski, A. F., Allred, J. C., Daw, A., Cauzzi, G., & Carlsson, M. 2017a, ApJ, 836, 12

Kowalski, A. F., Allred, J. C., Uitenbroek, H., et al. 2017b, ApJ, 837, 125
Kowalski, A. F., Cauzzi, G., & Fletcher, L. 2015a, ApJ, 798, 107
Kowalski, A. F., Hawley, S. L., Carlsson, M., et al. 2015b, SoPh, 290, 3487
Kowalski, A. F., Hawley, S. L., Holtzman, J. A., Wisniewski, J. P., & Hilton, E. J. 2012, SoPh, 277, 21
Kowalski, A. F., Hawley, S. L., Wisniewski, J. P., et al. 2013, ApJS, 207, 15
Kowalski, A. F., Mathioudakis, M., Hawley, S. L., et al. 2016, ApJ, 820, 95
Kowalski, A. F., Mathioudakis, M., & Hawley, S. L. 2018, arXiv:1810.07226
Kowalski, A. F., Wisniewski, J. P., Hawley, S. L., et al. 2019, ApJ, 871, 167
Kramida, A., Ralchenko, Yu., Reader, J. & NIST ASD Team 2018, NIST Atomic Spectra Database (ver. 5.6.1) (Gaithersburg, MD: National Institute of Standards and Technology), https://physics.nist.gov/asd
Krucker, S., Hudson, H. S., Jeffrey, N. L. S., et al. 2011, ApJ, 739, 96
Krucker, S., Saint-Hilaire, P., Hudson, H. S., et al. 2015, ApJ, 802, 19
Kurucz, R. L. 2018, in ASP Conf. Ser. 515, Workshop on Astrophysical Opacities (San Francisco, CA: ASP), 47
Kusano, K., Bamba, Y., Yamamoto, T. T., et al. 2012, ApJ, 760, 31
Lemen, J. R., Title, A. M., Akin, D. J., et al. 2012, SoPh, 275, 17
Li, X., Zhang, J., Yang, S., & Hou, Y. 2019, PASJ, 71, 14
Livshits, M. A., Badalian, O. G., Kosovichev, A. G., & Katsova, M. M. 1981, SoPh, 73, 269
Maehara, H., Shibayama, T., Notsu, S., et al. 2012, Natur, 485, 478
Martínez Oliveros, J.-C., Hudson, H. S., Hurford, G. J., et al. 2012, ApJL, 753, L26
Matthews, S. A., van Driel-Gesztelyi, L., Hudson, H. S., & Nitta, N. V. 2003, A&A, 409, 1107
Meegan, C., Lichti, G., Bhat, P. N., et al. 2009, ApJ, 702, 791
Mihalas, D. 1978, in Stellar Atmospheres, ed. G. Burbidge & M. Burbidge (2nd ed.; San Francisco, CA: W.H. Freeman and Company)
Milligan, R. O., Kerr, G. S., Dennis, B. R., et al. 2014, ApJ, 793, 70
Murphy, R. J., Share, G. H., Grove, J. E., et al. 1997, ApJ, 490, 883
Namekata, K., Sakaue, T., Watanabe, K., et al. 2017, ApJ, 851, 91
Nave, G., & Johansson, S. 2013, ApJS, 204, 1
Nave, G., Johansson, S., Learner, R. C. M., Thorne, A. P., & Brault, J. W. 1994, ApJS, 94, 221
Neidig, D. F. 1983, SoPh, 85, 285
Neidig, D. F., Kiplinger, A. L., Cohl, H. S., & Wiborg, P. H. 1993a, ApJ, 406, 306
Neidig, D. F., Wiborg, P. H., & Gilliam, L. B. 1993b, SoPh, 144, 169
Nishizuka, N., Asai, A., Takasaki, H., Kurokawa, H., & Shibata, K. 2009, ApJL, 694, L74
Osten, R. A., Kowalski, A., Drake, S. A., et al. 2016, ApJ, 832, 174
Penn, M., Krucker, S., Hudson, H., et al. 2016, ApJL, 819, L30
Procházka, O., Milligan, R. O., Allred, J. C., et al. 2017, ApJ, 837, 46
Procházka, O., Reid, A., Milligan, R. O., et al. 2018, ApJ, 862, 76
Rathore, B., & Carlsson, M. 2015, ApJ, 811, 80
Reep, J. W., & Russell, A. J. B. 2016, ApJL, 818, L20
Reep, J. W., Russell, A. J. B., Tarr, L. A., & Leake, J. E. 2018, ApJ, 853, 101
Rubio da Costa, F., Kleint, L., Petrosian, V., Liu, W., & Allred, J. C. 2016, ApJ, 827, 38
Russell, A. J. B., & Fletcher, L. 2013, ApJ, 765, 81
Rutten, R. J. 2003, Radiative Transfer in Stellar Atmospheres (Utrecht: Utrecht University)
Sadykov, V. M., Kosovichev, A. G., Sharykin, I. N., Zimovets, I. V., & Vargas Dominguez, S. 2016, ApJ, 828, 4
Sansonetti, C. J., & Nave, G. 2014, ApJS, 213, 28
Seaton, M. J. 1960, RPPh, 23, 313
Sharykin, I. N., & Kosovichev, A. G. 2014, ApJL, 788, L18
Silverberg, S. M., Kowalski, A. F., Davenport, J. R. A., et al. 2016, ApJ, 829, 129
Simões, P. J. A., Fletcher, L., Labrosse, N., & Kerr, G. S. 2016, in ASP Conf. Ser. 504, Coimbra Solar Physics Meeting: Ground-based Solar Observations in the Space Instrumentation Era, ed. I. Dorotovic, C. E. Fischer, & M. Temmer (San Francisco, CA: ASP), 197
Sirianni, M., Jee, M. J., Benítez, N., et al. 2005, PASP, 117, 1049
Tayal, S. S., & Zatsarinny, O. 2018, PhRvA, 98, 012706
Thalmann, J. K., Su, Y., Temmer, M., & Veronig, A. M. 2015, ApJL, 801, L23
Tian, H., Young, P. R., Reeves, K. K., et al. 2015, ApJ, 811, 139
Uitenbroek, H. 2001, ApJ, 557, 389
Vernazza, J. E., Avrett, E. H., & Loeser, R. 1981, ApJS, 45, 635
Veronig, A. M., & Brown, J. C. 2004, ApJL, 603, L117
Warmuth, A., & Mann, G. 2016, A&A, 588, A116
Watanabe, K., Kitagawa, J., & Masuda, S. 2017, ApJ, 850, 204
Wülser, J.-P., Jaeggli, S., De Pontieu, B., et al. 2018, SoPh, 293, 149
Zharkova, V. V., & Zharkov, S. I. 2007, ApJ, 664, 573